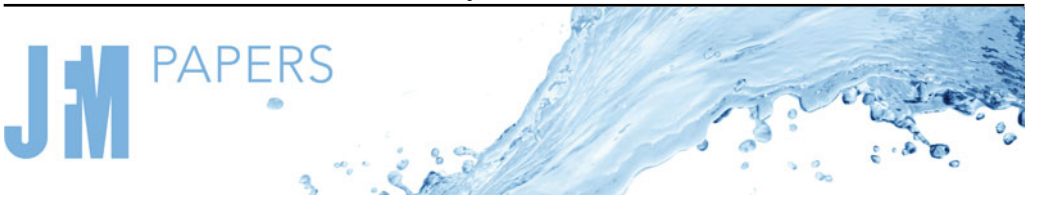
J. Fluid Mech. (2026), *vol.* 1038, A28, doi:10.1017/jfm.2026.11698



A model of unsteady line-vortex dynamics in free-surface gravity-wave flow

Tobias Bölle[1] **and Thomas Leweke**[2]

[1]Deutsches Zentrum für Luft- und Raumfahrt, Institut für Physik der Atmosphäre, Oberpfaffenhofen, Germany

[2]CNRS, Aix-Marseille Université, Centrale Méditerranée, IRPHE, Marseille 13384, France

Corresponding author: Tobias Bölle, tobias.boelle@dlr.de

(Received 15 October 2025 UTC; revised 27 March 2026 UTC; accepted 13 May 2026 UTC)

Meandering is the prototype of the unsteady dynamics of line vortices observed in experiments and has never been examined subject to free-surface gravity-wave flow explicitly before. With this study, we pursue the objective to make progress in developing a theoretical vortex-meandering model from first principles. As in recently proposed models, we start our modelling from the experimentally measurable vortex-centre integral, which we consider as the definition of vortex meandering. We then derive an equation of motion for the vortex centre assuming three-dimensional vorticity dynamics, which has not been reported in the literature previously. Considering meandering to correspond to the lateral displacement of the vortex as a whole, we demonstrate theoretically that practically all terms in this equation of motion mutually cancel and that the problem cannot be closed with the experimentally available two-dimensional data alone. As suggested by our analysis, we therefore assume vortex meandering to be associated with an infinity of viscously damped displacement waves excited by the free stream turbulence and propagating along the core. The resulting power spectrum closely resembles that of an Ornstein–Uhlenbeck process, as proposed recently. We compare all aspects and assumptions of our model development with an experiment of a single line vortex conducted in a free-surface recirculating water channel. The effect of the free-surface gravity wave on the vortex-meandering dynamics has not been examined before, but is found to have a non-negligible contribution of the same order as the free stream turbulence in the facility. Overall, we confirm our model assumptions and find remarkably good principal agreement between the model characteristics and the experiment at the 5 % level of significance. Despite this overall good agreement, there remains the considerable deficiency that the model-predicted vortex-response time scale is approximately two orders different from the experimental one. While the reason for this inconsistency is not clear yet,

© The Author(s), 2026. Published by Cambridge University Press. This is an Open Access article, distributed under the terms of the Creative Commons Attribution licence (https://creativecommons.org/licenses/by/4.0/), which permits unrestricted re-use, distribution and reproduction, provided the original article is properly cited.

the results are encouraging and hopefully help solving the problem of vortex meandering eventually.

Key words: vortex dynamics, Surface gravity waves, low-dimensional models

1. Introduction

Vortices and waves are arguably the most important building blocks of complex fluid flows. The evolution and dynamics of vortices in interface flows and in particular the associated wave–vortex interactions constitute a major canonical problem in fluid dynamics (Bühler 2010; McIntyre 2019). Important applications range from naval hydrodynamics (Sarpkaya & Neubert 1994; Chen & Chwang 2002; Curtis & Kalisch 2017) over aeronautics (Sarpkaya & Suthon 1991) to geophysics (Bühler 2010; van Heijst 2017). This prior research focused on vortices close to free surfaces, emphasising surface deformation processes (Curtis & Kalisch 2017), vortex instabilities (Archer, Thomas & Coleman 2010), wave refraction (Bühler 2010; McIntyre 2019) and interface entrainment (Linden 1973). Probably for reasons of experimental realisability and theoretical tractability, prior studies assumed (self-rising) vortex rings, two-dimensional vortex pairs or point vortices. In this study, we investigate the three-dimensional dynamics of an isolated line vortex that can be assumed sufficiently far from a free surface so as not to exert any appreciable effect on the free-surface wave dynamics. However, the surface impacts the vortex dynamics through a time-dependent boundary condition in the surrounding potential-flow field.

More specifically, this study focuses on the unsteady dynamics of a single slender line vortex, as it forms, e.g. in the wake of a lifting surface, perpetually excited by small-scale turbulence and free-surface gravity-wave flow. Besides potential relevance in the above applications, this is also an important abstraction of vortex experiments conducted in free-surface water channels (Baker *et al.* 1974; Bailey *et al.* 2018; Gutierrez-Castillo *et al.* 2022). In this setting, the vortex axis and the direction of wave propagation are aligned. The main manifestation of unsteady vortex dynamics observed in such experiments of line vortices is referred to as meandering (Jacquin *et al.* 2001; Bölle 2021). Despite numerous studies, its root cause and governing mechanisms are not fully understood (Edstrand *et al.* 2016; Bölle 2023; Wu *et al.* 2025). Candidate mechanisms have been reviewed and critically discussed recently by Bölle (2024).

While there is no rigorous definition of vortex meandering, it seems generally accepted that it refers to the lateral displacement of the vortex core as a whole (Devenport *et al.* 1996; Bölle 2021). Let r_c and t_v denote the characteristic length scale of the vortex core and the (slow) time scale of its response dynamics. It seems that a reasonable abstraction of typical experimental configurations would be a coherent vortex evolving in an incoherent environment filling a much larger container. That is, $r_c \ll \sqrt{M}$, if M is a measure of the cross-sectional area of the experimental facility and $t_v \gg t_r$, if t_r is a characteristic time scale of the surrounding small-scale disturbances in the facility. In this setting, if the vortex axis is aligned with the streamwise z-direction perpendicular to M, the vortex meandering kinematics are conveniently characterised by the motion of the vortex centre

$$X_\alpha(z,t) = \frac{1}{\Gamma}\int_M \mathrm{d}^2x\; x_\alpha w_z(\boldsymbol{x},z,t) \quad (\alpha = 1,2), \tag{1.1}$$

where $\Gamma = \int_M \mathrm{d}^2x\; w_z(\boldsymbol{x})$ denotes the circulation computed over the streamwise vorticity w_z in the fixed measurement plane M with coordinates x_α, $\alpha = 1, 2$ (Saffman 1995). We thus define meandering as the motion of the vortex centre and take (1.1) as the starting

point of our model development. We emphasise that (1.1) is a measurable quantity that can directly be computed from experimentally measured flow fields.

Experiments since the 1970s provide considerable evidence that vortex meandering has the following universal characteristics: the meandering motion is a centred random process with a Gaussian distribution and downstream-growing variance (Baker *et al.* 1974; Devenport *et al.* 1996; van Jaarsveld *et al.* 2011; Bailey *et al.* 2018; Dghim *et al.* 2020, 2021); the variance is distributed over the entire range of resolved scales with monotonically increasing levels towards low frequencies (Devenport *et al.* 1996; Jacquin *et al.* 2001; Bailey & Tavoularis 2008; Bölle 2023); vortex meandering is associated with a dipolar pattern in the fluctuation vorticity (Edstrand *et al.* 2016; Karami *et al.* 2019; Dghim, Ferchichi & Fellouah 2020; Bölle *et al.* 2023). Although this fluctuation–vorticity pattern and the downstream-growing variance suggest that meandering corresponds to some form of vortex instability, we are not aware of any experimental demonstration (e.g. Fabre & Jacquin 2004; Edstrand *et al.* 2016; Qiu *et al.* 2021; Bölle 2024). Rather, it appears that meandering manifests for stable vortices that are perpetually excited by surrounding vortical disturbances and unsteady potential flow. Although experiments were conducted in free-surface facilities (e.g. Baker *et al.* 1974; Del Pino *et al.* 2011; Bailey *et al.* 2018; Gutierrez-Castillo *et al.* 2022), the effect of gravity waves on the vortex-meandering motion has never been examined.

Taking (1.1) as an (operational) definition of vortex meandering, Bölle (2023) proposed a Brownian motion-like model in terms of an Ornstein–Uhlenbeck process. Systematically using tools from statistical inference, this model was shown to be consistent with experiments (Bölle 2024). However, these studies introduced essential parameters *ad hoc* from previous studies; in particular, the characteristic vortex response time scale t_v. Our main objective in this study is to make progress in this direction by deriving an equation of motion for (1.1) from first principles. Secondly, we want to put the Brownian-motion theory of Bölle (2023), and in particular our newly derived model, to test in a new and independent experiment, specifically designed for the analysis of vortex meandering, i.e. with a high spatial measurement resolution of the core region and a long time-resolved recording.

Assuming the vorticity dynamics to be strictly two-dimensional, it can be shown that the vortex centre moves with the external potential flow (Poincaré 1893; Saffman 1995). In particular, if there is no external flow and the velocity vanishes at infinity, the vortex centre is conserved (Batchelor 2000). This is incompatible with the experimentally confirmed fact that vortex meandering is at the same time apparently random and characterised by a stabilising intrinsic dynamics (Bölle 2021). Especially the latter intrinsic dynamics require the assumption of a three-dimensional vortex. However, (1.1) is not readily defined in three-dimensional flow (Saffman 1995). Three-dimensional generalisations of (1.1) have been proposed (Saffman 1995) and analogous equations of motion derived. However, they do not seem relevant here, as vortex meandering in experiments is characterised in terms of (1.1). We are therefore faced with the problem of three-dimensional vorticity dynamics which we characterise by the kinematics of a two-dimensional vortex-centre integral (1.1). To the best of our knowledge, this problem has not been treated previously, and no equation of motion for (1.1) in the case of three-dimensional vorticity distributions has been derived before.

While an accepted, quantitative theory of vortex meandering is not available today, the additional effect of wave dynamics has never been studied analytically or experimentally before. We hope that our approach constitutes a valuable first attempt to close this gap. Whereas a vortex-meandering model coupled to surface waves is rather obviously relevant for marine applications, it may also be pertinent for the interaction between aircraft trailing

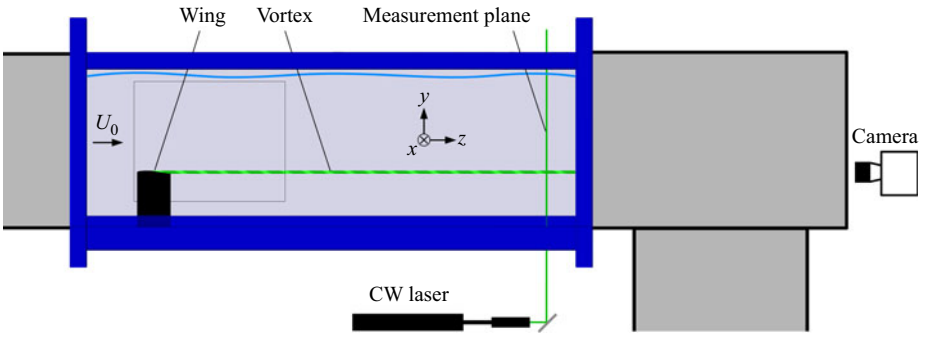


Figure 1. Schematic of the water channel experiment. The rectangle around the wing tip shows the area in which the flow in the empty channel was measured. The blue line represents the stationary deformed free surface for the present experimental conditions.

vortices and gravity waves in the atmosphere. In any case, it constitutes an important result for the interpretation of vortex experiments in free-surface facilities.

The paper is structured as follows. We present the experimental set-up and measurement procedure in § 2. The development of the meandering model is detailed in § 3, followed by a verification of the model characteristics with the experiment in § 4. The surface-wave effect is quantified and discussed in § 5. We discuss and summarise our main findings in § 6.

2. Vortex meandering experiment

2.1. *Set-up*

The vortex meandering experiment was carried out in a free-surface recirculating water channel with a test section of dimensions 150 cm (length) × 50 cm (height) × 38 cm (width), with a set-up similar to the one used by Roy *et al.* (2011), see figure 1. The vortex was generated by a rectangular airfoil made of polyvinyl chloride, with a NACA 0012 cross-section profile and a rounded tip with a varying tip diameter equal to the local thickness of the wing. The airfoil was mounted vertically on a U-frame positioned along the side and bottom boundaries of the channel, with the leading edge positioned 20 cm from the test section entry. The wing had a chord $c = 9.8$ and a 15 cm span, resulting in a vertical position of the tip vortex at approximately one third of the water height in the channel. This was chosen to limit the influence of the free surface, which exhibits a steady deformation at higher flow velocities (see movie 1 in the Supplementary material available at https://doi.org/10.1017/jfm.2026.11698). The airfoil was placed at an angle of attack of 9°.

2.2. *Free stream properties*

The characteristics of the free stream were determined by measuring the velocity field in the empty channel in a rectangular area around the position of the wing tip (figure 1), using particle image velocimetry (PIV). The mean free stream velocity for the current experiment was $U_0 = (79.1 \pm 0.3)$ cm s^{-1}, resulting in a chord-based Reynolds number $Re = U_0 c/\nu \approx 8 \times 10^4$, where ν is the kinematic viscosity of water. The time-averaged free stream velocity is spatially uniform to within 1 % and the turbulence intensity (Tu), determined by correcting for PIV noise and not including fluctuations related to the sloshing phenomenon described below, is close to 0.6 %.

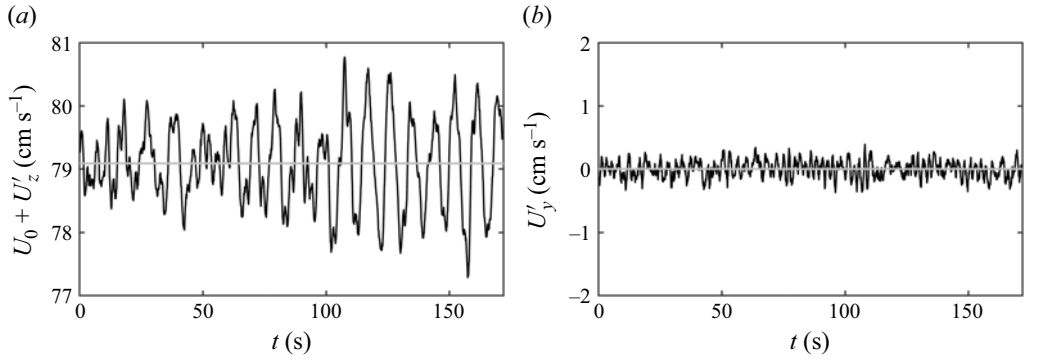


Figure 2. Time history of the (a) streamwise and (b) vertical component of the free stream velocity in the empty channel, measured at a height $y = 16.2$ cm above the channel floor. The respective time-mean velocities are shown by grey lines.

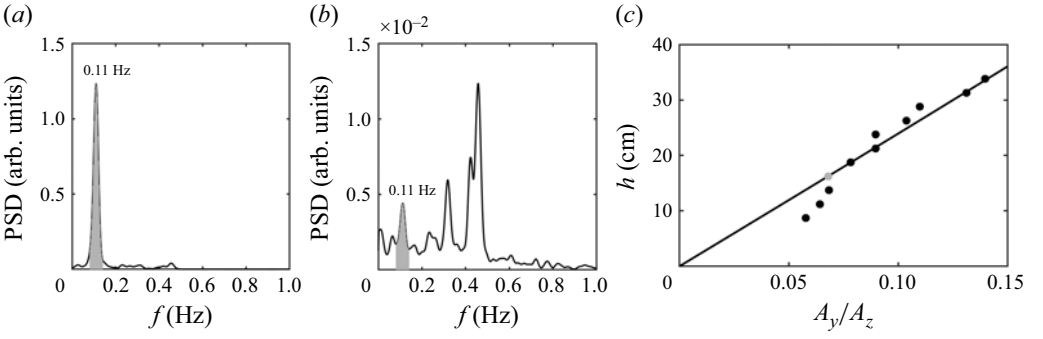


Figure 3. (a,b) Power spectral density (PSD) of the free stream velocities in figure 2. The grey areas represent the power contained in a small frequency band centred at the observed sloshing frequency. (c) Amplitude ratio of the velocity oscillations in the vertical and streamwise directions as a function of h. The grey dot represents the data in (a), (b) and figure 2, and the line the theoretical relation (2.2), with a fitted value $L = 7.5$ m.

A well-known phenomenon occurring in free-surface basins and channels is a low-frequency sloshing of the fluid (Ibrahim 2005), a gravity wave propagating back and forth between the extremities of the facility, with a wavelength given by twice its length. This small-amplitude oscillation is superposed on the steady recirculating flow in the channel. Figure 2 illustrates the sloshing in our facility by the time history of the streamwise and vertical velocity components, averaged over a horizontal strip of 2 cm width in the area shown in figure 1, at the height of the wing tip. A low-frequency oscillation is clearly present in the streamwise velocity, much less so in the vertical component. This is confirmed by the corresponding power spectra in figures 3(a) and 3(b). Movie 2 in the Supplementary material further demonstrates the sloshing motion, by showing the dominant mode of a dynamic mode decomposition of a series of PIV velocity fields.

For a rectangular container of depth d and length L, the sloshing frequency f_s is given by

$$f_s = \frac{1}{2\pi}\sqrt{\frac{\pi g}{L}\tanh\frac{\pi d}{L}}, \tag{2.1}$$

where g is the acceleration of gravity. With a water depth of $d = 45$ cm, the observed value of $f_s = 0.11$ Hz would correspond to a length $L = 9.5$ m, which is of the order of the

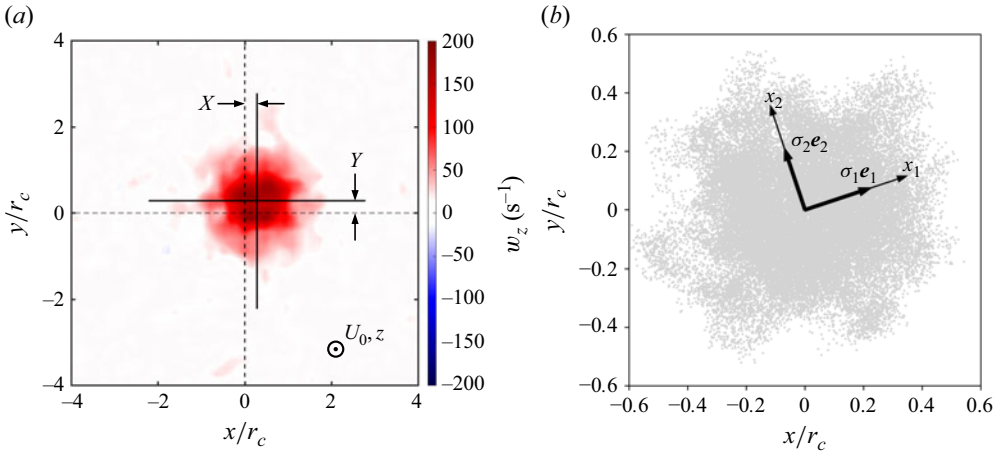


Figure 4. (*a*) Instantaneous vorticity field of the tip vortex at $z/c = 11.2$ (see also movie 3 in the Supplementary material). The origin represents the mean position of the vortex centre, and the black lines the instantaneous centre. The free stream velocity U_0 is out of the measurement plane along z, which together with x and y defines the laboratory-fixed reference frame. (*b*) Collection of all instantaneous vortex-centre positions of one recording (grey dots). The principal axes $\boldsymbol{e}_\alpha$ of this distribution define the principal-axes coordinate system x_α with standard deviations σ_α in the measurement plane.

overall dimension (6.5 m) of the channel (which is in fact not a rectangular container). For finite-depth free-surface gravity waves, the amplitude ratio of the horizontal and vertical velocity oscillations is a function of the vertical coordinate. If h is the distance from the rigid bottom, this ratio is given by

$$\frac{A_y}{A_z} = \tanh \frac{\pi h}{L}. \tag{2.2}$$

Experimentally, it can be estimated by the square root of the ratio of the areas underneath the spectral peaks corresponding to the sloshing motion (highlighted in grey in figures 3*a* and 3*b*). The result in figure 3(*c*) compares reasonably well with the theoretical prediction, assuming a container dimension $L = 7.5$ m, which is again compatible with the channel dimensions. The preceding results represent qualitative and, to a certain degree, quantitative evidence that a sloshing oscillation is present in our experimental facility, which must be taken into account in the further analysis of the tip-vortex dynamics.

2.3. *Structure and dynamics of the wing tip vortex*

The properties and motion of the wing tip vortex were measured in a plane perpendicular to the free stream located at a downstream distance $z/c = 11.2$ from the trailing edge of the wing. The transverse velocity field was measured using PIV at a frequency of 1 kHz. The flow was seeded with silver-coated hollow glass spheres of diameter 10 µm, and illumination was achieved with a 10 W continuous-wave (CW) solid-state fibre laser (Azurlight Systems). Images were recorded by a Phantom VEO 410L high-speed digital camera and processed by an in-house algorithm (Meunier & Leweke 2003; Aguilar-Cabello, Parras & del Pino 2022). A total of $N = 38\,266$ velocity fields was obtained, covering a time interval of 38.3 s.

Figure 4(*a*) shows an example of the instantaneous vorticity distribution of the tip vortex in the measurement plane. The vortex centre (X,Y), indicated by the black lines, was found using (1.1) for the vorticity centroid. Only vorticity values larger than 50 % of the

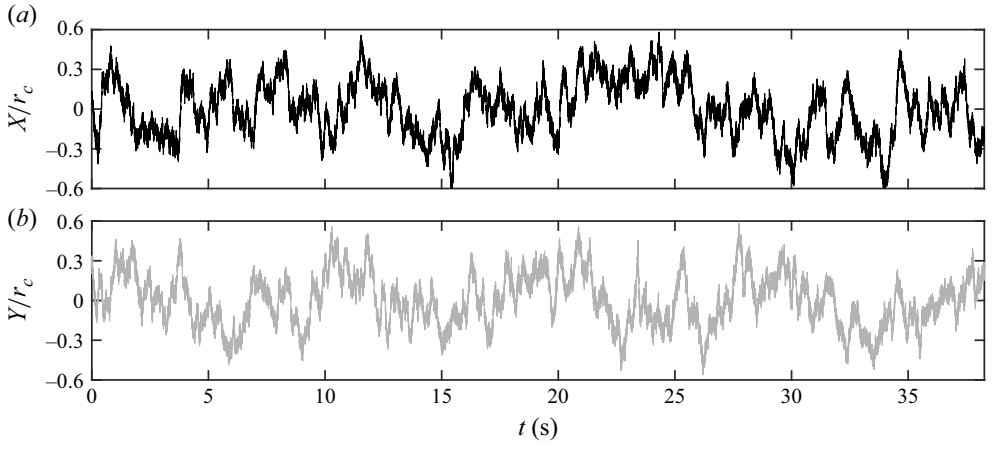


Figure 5. Time history of the (*a*) horizontal and (*b*) vertical vortex displacement.

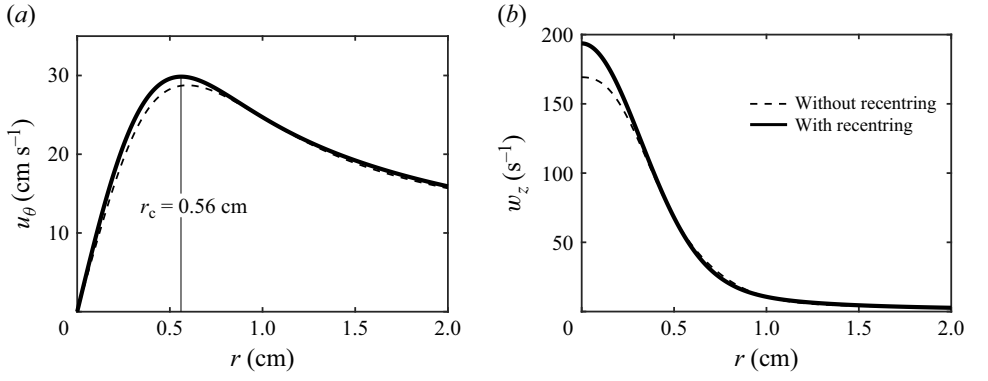


Figure 6. Radial profiles of the (*a*) mean azimuthal velocity and (*b*) axial vorticity of the wing tip vortex at $z/c = 11.2$. The dashed lines, representing $\overline{u}_\theta$ and $\overline{w}_z$, were obtained from the average velocity field of all 38 266 measurements. For the solid lines, representing $\mathfrak{u}_\theta$ and $\mathfrak{w}_z$ (see § 3.2), 5000 fields were averaged after recentring the vortex, using the displacement data in figure 5.

maximum vorticity were taken into account, in order to reduce the effect of low-level vorticity at large distances from the centre, that are mostly due to noise from the PIV method. A time sequence of the vorticity field illustrating the meandering motion can be seen in movie 3 of the Supplementary material. In figure 4(*b*), the instantaneous positions from the entire time series are collected. This figure also shows the vortex-centre principal-axes system x_1, x_2 used in the analysis in § 3. An example of the time history of the vortex position is presented in figure 5.

The structure of the tip vortex was determined from the time-averaged velocity field. Velocities were interpolated onto a polar grid around the vortex centre to determine the radial profile of the azimuthally averaged azimuthal velocity and axial vorticity. The results for a time average relative to the mean vortex centre are shown in figure 6 as dashed lines. The core radius r_c, which is a characteristic length scale of the vortex (used to non-dimensionalise the coordinates in figures 4 and 5), is defined as the radius of the maximum azimuthal velocity. The meandering motion of the vortex leads to an apparent larger core radius and lower maximum vorticity (Baker *et al.* 1974; Devenport *et al.* 1996). This effect can be eliminated by recenterng each velocity field according to the

measured instantaneous vortex displacement (figure 5) before averaging (Heyes, Jones & Smith 2004). The corresponding results in figure 6 (solid lines) indeed reveal a larger maximum vorticity and smaller core size. The latter is determined as $r_c = 0.56$ cm for the present experiment. The analysis of Devenport *et al.* (1996) (see also § 3.2) for a Batchelor vortex subject to a two-dimensional Gaussian meandering motion of amplitude (standard deviation) σ, predicts an increase of the measured core radius by a factor $\sqrt{(1 + 2\kappa\sigma^2/r_c^2)}$, and a decrease of the vorticity maximum by a factor $(1 + 2\kappa\sigma^2/r_c^2)^{-1}$, with $\kappa = 1.25643$. From the data in figure 5, we find $\sigma \approx 0.11$ cm. The corresponding predicted core radius increase of 5 % and vorticity decrease of 9 % are in good agreement with the measurements in figure 6.

The measured azimuthal velocity profile, corrected for the meandering motion, is extremely close to the theoretical distribution derived by Moore & Saffman (1973) for laminar vortices resulting from the vortex sheet roll-up behind a lifting surface,

$$\mathrm{u}_\theta = \frac{\beta}{a^n}\Gamma\left(\frac{3-n}{2}\right)\frac{r}{a}\,{}_1F_1\left(\frac{1+n}{2}, 2, -\frac{r^2}{a^2}\right), \tag{2.3}$$

where Γ is here the gamma function (not to be confused with the vortex circulation Γ) and ${}_1F_1$ the confluent hypergeometric function of the first kind. The radial length scale a is proportional to the core radius r_c and the parameters β and n represent the vortex strength (circulation) and the outer velocity profile structure ($\mathrm{u}_\theta \sim r^{-n}$, $r/a \gg 1$). For the current experiments, we find $a = 0.43$ cm, $\beta = 25.6\,\mathrm{cm}^{(n+1)}\,\mathrm{s}^{-1}$ and $n = 0.67$.

The current measurements can be compared with the turbulence-induced meandering amplitude proposed by van Jaarsveld *et al.* (2011): $\sigma_t/r_c \approx 4\,Tu\,\sqrt{zU_0/\Gamma}$. For the experimental parameter values ($Tu = 6 \times 10^{-3}$, $z = 110$ cm, $U_0 = 79.1\,\mathrm{cm\,s^{-1}}$, $\Gamma = 270\,\mathrm{cm^2\,s^{-1}}$), the formula predicts $\sigma_t/r_c \approx 0.14$, whereas the total meandering amplitude is $\sigma/r_c = 0.20$. It is shown in § 5.1 below that the sloshing wave is responsible for a vortex displacement of the same order as the turbulence-induced meandering. Both contribute to the measured total amplitude.

Overall, the vortex structure and meandering dynamics observed in the present experiments are all consistent with previous results reported in the literature.

3. Model for vortex meandering in a free-surface flow

We assume Cartesian coordinates $(\boldsymbol{x}, z)$, such that z is positive in the direction of the free stream velocity U_0, and $\boldsymbol{x}$ any system of two-dimensional Cartesian coordinates in the measurement plane M, centred on the mean vortex-centre location (figure 4). Vorticity is denoted by $w_i(\boldsymbol{x}, z, t)$, $i = 1, 2, 3$, with $w_3 = w_z$, and t denotes time. Assuming the vorticity to be a stationary random field, we introduce the Reynolds decomposition $w_i(\boldsymbol{x}, z, t) = \overline{w}_i(\boldsymbol{x}, z) + w_i'(\boldsymbol{x}, z, t)$, where $\overline{w}_i(\boldsymbol{x}, z)$ and $w_i'(\boldsymbol{x}, z, t)$ denote the time mean and fluctuation, respectively. An analogous Reynolds decomposition of the velocity reads $v_i(\boldsymbol{x}, z, t) = \overline{v}_i(\boldsymbol{x}) + v_i'(\boldsymbol{x}, z, t)$. The experiment suggests the formation of an isolated line vortex. Consequently, we assume the mean vorticity $\overline{w}_i(\boldsymbol{x}, z)$ to be effectively confined to a slender tubular region along z. The Helmholtz decomposition of the mean velocity reads $\overline{v}_i(\boldsymbol{x}, z) = U_0\delta_{iz} + \overline{u}_i(\boldsymbol{x}, z)$, whereas $\overline{w}_i = \varepsilon_{ijk}\partial\overline{u}_k/\partial x_j$. Herein, δ_{ij} and ε_{ijk} are the Kronecker delta and the three-dimensional Levi–Civita symbol, respectively, and the Einstein summation convention over repeated indices is assumed here and in the following, unless stated otherwise.

3.1. *General evolution equation for the vortex centre*

In this study, we are concerned with the apparently random lateral motion of the vortex as a whole, referred to as meandering. These vortex kinematics are conveniently described by the leading integrals of the vorticity field in the measurement plane, recalled here from (1.1) for convenience,

$$\Gamma(z,t)=\int_M \mathrm{d}^2x\; w_z(\boldsymbol{x},z,t),\qquad X_\alpha(z,t)=\frac{1}{\Gamma}\int_M \mathrm{d}^2x\; x_\alpha w_z(\boldsymbol{x},z,t)\quad(\alpha=1,2).\tag{3.1}$$

These integrals give the circulation Γ and the vortex centre coordinates X_α, respectively. We then define vortex meandering as the motion of the vortex centre $X_\alpha(z,t)$ in time, at a given position z. Inserting the Reynolds decomposition into (3.1) and respecting the characteristic symmetries of the vorticity field yields the leading-order approximations (Bölle 2023, 2024)

$$\Gamma=\int_M \mathrm{d}^2x\; \overline{w}_z(\boldsymbol{x}),\qquad X_\alpha(z,t)=\frac{1}{\Gamma}\int_M \mathrm{d}^2x\; x_\alpha w_z'(\boldsymbol{x},z,t)\quad(\alpha=1,2).\tag{3.2}$$

The measurement plane M is a non-material area containing the respective z-slice of the unsteady vortex over the entire measurement time. The mean vorticity distribution spreads downstream, as a consequence of the meandering motion (see § 3.2 and Baker *et al.* (1974) and Devenport *et al.* (1996) for details). We suppose that M is chosen large enough to contain the spreading mean vortex and therefore the circulation does not change appreciably downstream.

In the following, we work in the vortex-centre principal-axes system $x_i=(x_\alpha,z)=(x_1,x_2,z)=(\boldsymbol{x},z)$ spanned by the $\boldsymbol{e}_\alpha$ and $\boldsymbol{e}_z$ (figure 4*b*). In summations and products, Greek indices ($\alpha,\beta,\ldots$) take on values 1 and 2, whereas roman indices run from 1 to 3.

To derive the equation of motion for the vortex-meandering dynamics, we take the temporal derivative of (3.2). Since the integration domain M is non-material, derivation and integration commute (Batchelor 2000) and we obtain

$$\begin{aligned}\frac{\partial X_\alpha}{\partial t}&=\frac{1}{\Gamma}\int_M \mathrm{d}^2x\; x_\alpha\frac{\partial w_z'}{\partial t}\\&=\frac{1}{\Gamma}\int_M \mathrm{d}^2x\; x_\alpha\left[\overline{w}_i\frac{\partial v_z'}{\partial x_i}+w_i'\frac{\partial \overline{u}_z}{\partial x_i}-U_0\frac{\partial w_z'}{\partial z}-\overline{u}_i\frac{\partial w_z'}{\partial x_i}-v_i'\frac{\partial \overline{w}_z}{\partial x_i}\right]+\xi_\alpha(z,t).\end{aligned}\tag{3.3}$$

In the second line of (3.3), we have used the linearised fluctuation vorticity equation of an incompressible, inviscid fluid (Saffman 1995; Batchelor 2000). The forcing $\xi_\alpha(t)$ may represent the net effect of the omitted nonlinear advection terms or any externally applied excitation (Bölle *et al.* 2021).

Vortex eigenmodes with non-zero axial wavenumbers have an exponential decay in the radial coordinate (Ash & Khorrami 1995; Fabre & Jacquin 2004). This effectively compact support is also empirically observed for the leading proper orthogonal decomposition (POD) modes of the experimental velocity and vorticity fields (see figures 10 and 12). We therefore assume that the fluctuation fields in (3.3) vanish on the integration boundary ∂M. Further recalling that the velocity and vorticity fields are solenoidal, the equation of motion (3.3) can be simplified through integration by parts, yielding

$$\frac{\partial X_\alpha}{\partial t}=-U_0\frac{\partial}{\partial z}\frac{1}{\Gamma}\int_M \mathrm{d}^2x\; x_\alpha w_z'+\frac{1}{\Gamma}\int_M \mathrm{d}^2x\left[\overline{u}_\alpha w_z'+\overline{w}_z v_\alpha'-\overline{w}_\alpha v_z'-\overline{u}_z w_\alpha'\right]+\xi_\alpha(z,t).\tag{3.4}$$

We now assume a Helmholtz decomposition of the fluctuation-velocity fields $v_i' = U_i' + u_i'$, denoting the potential and rotational flow components by capital and lower-case letters, respectively. The former represent an external forcing and will be related to the free-surface gravity-wave flow present in the water channel experiment (see §§ 2.2 and 5.1). The latter relate to the fluctuation velocity field of the vortex. With this, the equation of motion of the vortex centre reads

$$\begin{aligned}\frac{\partial X_\alpha}{\partial t} + U_0\frac{\partial X_\alpha}{\partial z} = {} & \frac{1}{\Gamma}\int_M \mathrm{d}^2x\, \overline{u}_\alpha w_z' + \frac{1}{\Gamma}\int_M \mathrm{d}^2x\, \overline{w}_z u_\alpha' + \frac{1}{\Gamma}\int_M \mathrm{d}^2x\, \overline{w}_z U_\alpha' \\ & - \frac{1}{\Gamma}\int_M \mathrm{d}^2x\, \overline{u}_z w_\alpha' - \frac{1}{\Gamma}\int_M \mathrm{d}^2x\, \overline{w}_\alpha u_z' - \frac{1}{\Gamma}\int_M \mathrm{d}^2x\, \overline{w}_\alpha U_z' \\ & + \xi_\alpha(z,t). \end{aligned} \tag{3.5}$$

This shows that vortex meandering X_α, while being advected at the free stream velocity U_0, is principally subject to various feedback or forcing mechanisms appearing on the right-hand side of (3.5). These are organised such that the first line of (3.5) contains all terms that may affect a mean vortex with infinite swirl number (e.g. a Lamb–Oseen vortex (Fabre, Sipp & Jacquin 2006)). The second line comprises the additional terms for vortices with axial core flow (finite swirl numbers, e.g. Batchelor or Moore–Saffman vortices (Moore & Saffman 1973; Batchelor 2000)). The last forcing ξ_α is assumed to apply in both cases unchanged. To proceed, we have to evaluate the model integrals in (3.5). We do this analytically in the following § 3.2 and check the consistency of this result with our experiment in § 4.2.

3.2. *Analytical evaluation of the model integrals*

Our further evaluation is based on the fundamental conjecture that due to vortex meandering we have the two representations

$$w_z(\boldsymbol{x}, z, t) = \overline{w}_z(\boldsymbol{x}, z) + w_z'(\boldsymbol{x}, z, t) = \mathfrak{w}_z(\boldsymbol{x} - \boldsymbol{X}(z,t), z) \tag{3.6}$$

of the instantaneous flow fields. We here consider in detail only the streamwise vorticity; other vorticity or velocity components can be treated equivalently. The first representation is a Reynolds decomposition of the random flow field, as introduced above. We refer to the second as the vortex-meandering postulate: vortex meandering corresponds to a laminar (turbulent) vortex $\mathfrak{w}_z$ being displaced laterally as a whole (Baker *et al.* 1974; Bölle 2021). The instantaneous vortex-centre position is denoted $\boldsymbol{X}(z,t)$ and constitutes a stationary random process with probability density $p(\boldsymbol{X}_0|\boldsymbol{X}, z)$, where $\boldsymbol{X}_0 = \boldsymbol{X}(z=0)$. The standard deviations associated with the components X_α are denoted σ_α and are commonly referred to as meandering amplitudes. With respect to the experimental configuration, we are interested in the dynamics of the vortical flow at a fixed downstream position $z = z_M \neq 0$. For convenience, we therefore drop the reference to z in the following equations. We impose the compatibility condition (Baker *et al.* 1974; Devenport *et al.* 1996)

$$\int_{\mathbb{R}^2} \mathrm{d}^2X\; p(\boldsymbol{X})\mathfrak{w}_z(\boldsymbol{x} - \boldsymbol{X}) = \overline{w}_z(\boldsymbol{x}). \tag{3.7}$$

In particular, for a Gaussian vortex $\mathfrak{w}_z(\boldsymbol{x}) = 2\Omega_0 \exp(-|\boldsymbol{x}|^2/r_0^2)$, where Ω_0 is the fluid angular velocity at the vortex centre, r_0 the Gaussian core radius and $|\boldsymbol{x}|^2 := x_1^2 + x_2^2$ denotes the Euclidean vector norm. When subject to meandering obeying a Gaussian distribution p with standard deviations σ_α along the principal axes x_α, the mean

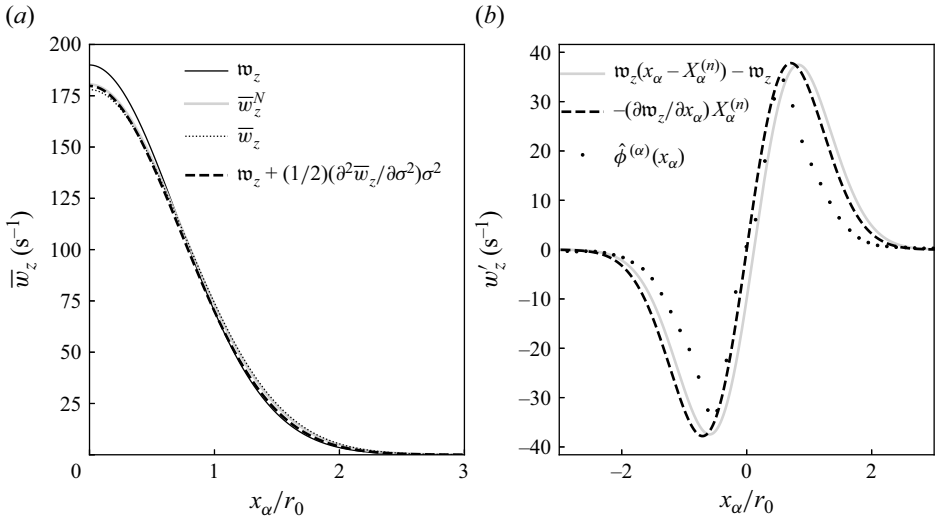


Figure 7. Comparison between meandering postulate and experiment. (*a*) Effect of vortex meandering on mean vorticity distribution. (*b*) Fluctuation vorticity associated with a typical vortex displacement $X_\alpha/r_c = 0.2$, compared with the first-order approximation in (3.11) and the leading POD mode $\hat{\phi}^{(\alpha)}$ profile along x_α (see § 4.1).

streamwise vorticity becomes

$$\overline{w}_z(\boldsymbol{x};\boldsymbol{\sigma}) = 2\Omega_0 r_0^2 \prod_{\alpha=1}^{2} \frac{\mathrm{e}^{-\frac{x_\alpha^2}{r_0^2+2\sigma_\alpha^2}}}{\sqrt{r_0^2+2\sigma_\alpha^2}}. \tag{3.8}$$

There is ample experimental evidence for the Gaussian distribution of vortex meandering in this (figure 13) and previous studies (Bailey & Tavoularis 2008; Dghim *et al.* 2020, 2021; Bölle 2024). For this specific case of a Gaussian vortex subject to meandering obeying a Gaussian probability distribution, series expansion of (3.8) in the standard deviation (meandering amplitude) σ_α, and using $\overline{w}_z(\boldsymbol{x};\boldsymbol{\sigma}=0) = \mathfrak{w}_z(\boldsymbol{x})$, yields

$$\begin{aligned}\overline{w}_z(\boldsymbol{x};\boldsymbol{\sigma}) &= \mathfrak{w}_z(\boldsymbol{x}) + \frac{1}{2}\frac{\partial^2\overline{w}_z}{\partial\sigma_\alpha^2}\bigg|_{\sigma_\alpha=0}\sigma_\alpha^2 + O\left(\boldsymbol{\sigma}^4\right)\\ &= \mathfrak{w}_z(\boldsymbol{x}) + \mathfrak{w}_z(\boldsymbol{x})\left(\frac{|\boldsymbol{x}|^2}{r_0^2} - 1\right)\left|\frac{\boldsymbol{\sigma}}{r_0}\right|^2 + O\left(\boldsymbol{\sigma}^4\right)\end{aligned} \tag{3.9}$$

for the leading-order representation of the mean flow as a consequence of meandering.

We tested the validity of these results empirically by a numerical experiment as follows. A Gaussian vortex $\mathfrak{w}_z$ is subjected to a Gaussian stochastic meandering $X_\alpha^{(n)} \sim \mathcal{N}(0, \sigma_\alpha/r_0)$, $n = 1, 2, \ldots, N$. The values of the parameters Ω_0, r_0 and σ_α were determined from the experiment (see § 2.3, $r_0 \approx r_c/1.12$ for a Gaussian vortex). A sample of $N = 10^5$ displaced vortices is generated with an ensemble mean $\overline{w}_z^N = N^{-1}\sum_{n=1}^{N}\mathfrak{w}_z((x_\alpha - X_\alpha^{(n)})/r_0)$. This mean estimator is compared in figure 7(*a*) with $\overline{w}_z$ according to (3.8) and with the leading-order approximation (3.9), showing very good agreement.

The meandering postulate (3.6), together with the compatibility condition (3.7), imply that fluctuations associated with the meandering motion have to vanish on average, i.e.

$$\int_{\mathbb{R}^2} \mathrm{d}^2 X p(\boldsymbol{X}) w_z'(\boldsymbol{x}, t) = 0 \implies w_z'(\boldsymbol{x}, t) = c_\alpha(\boldsymbol{x}) X_\alpha(t) + O\big(\boldsymbol{X}^3\big), \tag{3.10}$$

where the $c_\alpha(\boldsymbol{x})$ are stationary scalar fields. We assume that $p(\boldsymbol{X})$ is symmetric around the origin, which rules out any systematic meandering bias, i.e. neither positive nor negative vortex displacements are preferred on average. It follows immediately that the fluctuation vorticity associated with meandering must be an odd function of the instantaneous vortex centre position. All even terms, including a constant, have to vanish, since otherwise (3.10) cannot average to zero.

Using the meandering postulate (3.6) along with expansion (3.9) of the mean flow, we obtain the leading-order series expansion of the fluctuation vorticity

$$\begin{aligned} w_z'(\boldsymbol{x}, t) &= \mathfrak{w}_z(\boldsymbol{x} - \boldsymbol{X}(t)) - \overline{w}_z(\boldsymbol{x}; \boldsymbol{\sigma}) \\ &= -\frac{\partial \mathfrak{w}_z}{\partial x_\alpha} X_\alpha + \frac{1}{2}\frac{\partial^2 \mathfrak{w}_z}{\partial x_\alpha^2} X_\alpha^2 - \frac{1}{2}\frac{\partial^2 \overline{w}_z}{\partial \sigma_\alpha^2}\bigg|_{\sigma_\alpha = 0} \sigma_\alpha^2 + O\big(\boldsymbol{X}^3\big) + O\big(\boldsymbol{\sigma}^4\big). \end{aligned} \tag{3.11}$$

The first term of this result is consistent with the general functional structure of the fluctuation field anticipated in (3.10). However, the third term, contributed from (3.9), is non-random, non-zero and symmetric. It can therefore not vanish upon averaging with $p(\boldsymbol{X})$. Taking the average of (3.11) with respect to $p(\boldsymbol{X})$, we have

$$\begin{aligned} 0 &= \left[\frac{\partial^2 \mathfrak{w}_z}{\partial x_\alpha^2} - \frac{\partial^2 \overline{w}_z}{\partial \sigma_\alpha^2}\bigg|_{\sigma_\alpha = 0}\right] \frac{\sigma_\alpha^2}{2} + O\big(\boldsymbol{\sigma}^4\big) \\ &= \left[\mathfrak{w}_z\left(2x_\alpha^2 - 1\right) - \mathfrak{w}_z\left(x_\alpha^2 - 1\right)\right] \sigma_\alpha^2 + O\big(\boldsymbol{\sigma}^4\big) = \mathfrak{w}_z x_\alpha^2 \sigma_\alpha^2 + O\big(\boldsymbol{\sigma}^4\big), \end{aligned} \tag{3.12}$$

where we used that $\overline{X_\alpha^2} = \sigma_\alpha^2$ and that $\overline{X^{2n+1}} = 0$, $n \in \mathbb{N}_0$. The evaluation in the second line of (3.12) is for a Gaussian vortex subject to Gaussian meandering. Apparently, the second-order terms in (3.11) have a very similar, though not identical, functional structure. Consequently, they do not cancel identically and, in order to fulfil (3.10), must be cancelled by the higher-order even terms. We checked these results empirically, again by generating a set of 10^5 vorticity fields using a Gaussian distribution of displacements. The sample mean of w_z' indeed vanishes within machine accuracy.

For meandering amplitudes σ_α much smaller than the core radius r_c, we can neglect second-order terms in (3.9) and (3.11). For the present experiment $\sigma_\alpha / r_c \sim 10^{-1}$ (§ 4.3), which is a typical value for meandering amplitudes (Devenport *et al.* 1996; Bailey & Tavoularis 2008; van Jaarsveld *et al.* 2011; Bölle 2021). We therefore assume the leading-order, linear approximation $\overline{w}_z = \mathfrak{w}_z$ and $w_z' = -(\partial \mathfrak{w}_z / \partial x_\beta) X_\beta$ (see figure 7) and alike for all other mean and fluctuation fields from now on. Inserting these expressions into (3.5) yields

$$\begin{aligned} \frac{\partial X_\alpha}{\partial t} + U_0 \frac{\partial X_\alpha}{\partial z} = &-\frac{1}{\Gamma}\int_M \mathrm{d}^2 x \left(\mathfrak{u}_\alpha \frac{\partial \mathfrak{w}_z}{\partial x_\beta}\right) X_\beta - \frac{1}{\Gamma}\int_M \mathrm{d}^2 x \left(\mathfrak{w}_z \frac{\partial \mathfrak{u}_\alpha}{\partial x_\beta}\right) X_\beta \\ &+ \frac{1}{\Gamma}\int_M \mathrm{d}^2 x \left(\mathfrak{u}_z \frac{\partial \mathfrak{w}_\alpha}{\partial x_\beta}\right) X_\beta + \frac{1}{\Gamma}\int_M \mathrm{d}^2 x \left(\mathfrak{w}_\alpha \frac{\partial \mathfrak{u}_z}{\partial x_\beta}\right) X_\beta \\ &+ \frac{1}{\Gamma}\int_M \mathrm{d}^2 x\, \mathfrak{w}_z U_\alpha' - \frac{1}{\Gamma}\int_M \mathrm{d}^2 x\, \mathfrak{w}_\alpha U_z' + \xi_\alpha(z, t). \end{aligned} \tag{3.13}$$

Integration by parts of the first and second integrals in (3.13) and assuming that the laminar vortex has effectively compact support in M (Saffman 1995), it readily follows that the integrals in the first and second line of (3.13) cancel mutually. The last line of (3.13) contains the external forcing U_i' due to linear potential flow (i.e. boundary effects) and otherwise neglected vortical nonlinearities. At this point there is no conceptual difference between these three terms, so that we assemble them into one generic forcing f_α. With this, the final problem of vortex meandering becomes

$$\frac{\partial X_\alpha}{\partial t} = -U_0 \frac{\partial X_\alpha}{\partial z} + f_\alpha(z,t), \quad 0 \le z < \infty, \quad -\infty < t < \infty, \tag{3.14}$$

$$\text{initial condition}, \quad X_\alpha(z, t = t_0) = I_\alpha(z) \tag{3.15}$$

$$\text{boundary (inflow) condition}, \quad X_\alpha(z = 0, t) = X_{0\alpha}(t). \tag{3.16}$$

This is a spatiotemporally forced advection problem in which initial perturbations $X_{0\alpha}$ at $z = 0$ are transported along the characteristic defined by the free stream velocity U_0. In a frame moving with the free stream, perturbations are continuously amplified and grow without bound on average (Wiener process). This is not realistic and does not reflect the fact that vortices have a response dynamics in the form of eigenmodes propagating along the vortex. For typical experimental configurations, vortices are in a linearly stable regime and all eigenmodes are damped (Edstrand *et al.* 2016; Qiu *et al.* 2021; Bölle *et al.* 2023; Bölle 2024).

3.3. *General solution of the vortex-meandering equation of motion*

In this section, we derive the general solution of the above meandering problem under the assumption that the actual response dynamics is given by an infinity of vortex eigenmodes subject to advection by the free stream flow. Vortex meandering as described by (3.14)–(3.16) is a stationary, spatial problem. For its solution, we therefore assume a Laplace transform in space (denoted $\tilde{(\cdot)}$) and Fourier transform in time (denoted $\hat{(\cdot)}$). This yields

$$\hat{\tilde{X}}_\alpha(s,\omega) = \frac{\hat{\tilde{f}}_\alpha(s,\omega) + U_0 \hat{X}_{0\alpha}(\omega)}{\mathrm{i}(\omega_a + \omega_v) + sU_0} = \frac{1}{U_0} \frac{\hat{\tilde{f}}_\alpha(s,\omega) + U_0 \hat{X}_{0\alpha}(\omega)}{\mathrm{i}U_0^{-1}(\omega_a + \omega_v) + s}, \tag{3.17}$$

where $\omega = \omega_a + \omega_v$ denotes the real frequency, having a contribution ω_a from the advection at U_0 and an intrinsic dynamics ω_v in terms of eigenmodes propagating along the vortex core. The complex frequency from the Laplace transform is denoted $s = \varsigma_s + \mathrm{i}k$, with ς_s and k denoting the spatial damping rate and wavenumber, respectively. Taking the inverse Laplace transform of (3.17) yields the general equation of motion for the downstream evolution of the temporal Fourier amplitudes

$$\hat{X}_\alpha(z,\omega) - \hat{X}_{0\alpha}(\omega) e^{-\mathrm{i}\frac{\omega}{U_0}z} e^{-\varsigma_s z} = \int_0^z \mathrm{d}z'\, e^{-\varsigma_s (z-z')} e^{-\mathrm{i}\frac{\omega}{U_0}(z-z')} \frac{\hat{f}(z',\omega)}{U_0}. \tag{3.18}$$

We note that the spectral damping ς_s and intrinsic frequencies ω_v are arbitrary in this solution and are fully determined by the eigenmodes associated with vortex meandering.

For now, let us ignore any forcing by potential flow and assume a vortex embedded in the residual turbulence of the experimental facility. (This being permitted due to the linearity of the problem.) We assume the surrounding turbulence to be of much smaller scale than the vortex response. This allows us to model the forcing exerted by the turbulence on the vortex as a sequence of spatiotemporally uncorrelated Dirac impacts. We therefore assume the 'Langevin' condition on the forcing (an asterisk denotes complex conjugation)

$$\overline{\hat{\tilde{\xi}}}(z,\omega) = 0, \quad \overline{\hat{\tilde{\xi}}(z,\omega)\hat{\tilde{\xi}}^*(z',\omega')} = 2D\delta(\omega - \omega')\delta(z - z'), \tag{3.19}$$

stating that the forcing balances on average and that a Dirac-localised forcing ξ excites all wavenumbers and frequencies equally with an amplitude parameter D. Averaging (3.18) using this assumption, the mean becomes

$$\overline{\hat{X}}_\alpha(z,\omega) = \hat{X}_{0\alpha}(\omega) e^{-\mathrm{i}\frac{\omega}{U_0}z} e^{-\varsigma_s z}, \tag{3.20}$$

given that the inflow condition $X_{0\alpha}$ is a sure event. We notice that (3.20) corresponds to the homogeneous solution of (3.18). Introducing the fluctuation around the mean $\hat{X}'_\alpha(z,\omega) = \hat{X}_\alpha(z,\omega) - \overline{\hat{X}}_\alpha(z,\omega)$ and comparing with (3.18) shows that the fluctuation can be identified with the particular solution. The variance follows from

$$\begin{aligned}
\overline{|\hat{X}'_\alpha|^2}(z,\omega) &= \int_0^z \mathrm{d}z' \int_0^z \mathrm{d}z'' e^{-\varsigma_s(z-z')} e^{-\varsigma_s(z-z'')} e^{-\mathrm{i}\frac{\omega}{U_0}(z-z')} e^{\mathrm{i}\frac{\omega}{U_0}(z-z'')} \frac{\overline{\hat{\xi}(z',\omega)\hat{\xi}^*(z'',\omega)}}{U_0^2} \\
&= 2\frac{D}{U_0^2} e^{-2\varsigma_s z} \int_0^z \mathrm{d}z' \int_0^z \mathrm{d}z'' \, e^{\varsigma_s(z'+z'')} e^{\mathrm{i}\frac{\omega}{U_0}(z'-z'')} \delta(z'-z'') \\
&= 2\frac{D}{U_0^2} e^{-2\varsigma_s z} \int_0^z \mathrm{d}z' \, e^{2\varsigma_s z'} = \frac{D}{U_0^2\varsigma_s}\left[1 - e^{-2\varsigma_s z}\right].
\end{aligned} \tag{3.21}$$

In experiments, we measure the temporal variation of X_α in a fixed measurement plane at $z = z_M$. The streamwise gradient in this measurement plane, appearing on the right-hand side of (3.14), should reflect these internal dynamics due to excitation of vortex eigenmodes. This is reflected in the solution (3.20) and (3.21) by spatially evolving eigenmodes. However, streamwise gradients and streamwise propagating eigenmodes cannot be inferred from our experiment and have to be estimated from theory.

3.4. *Estimation from the dispersion relation of the Moore–Saffman vortex*

As formalised in (3.2), the instantaneous vortex-centre position is a weighted average of the stochastic fluctuation vorticity w'_z in a Reynolds decomposition. Consequently, our derivation of the vortex-meandering equation of motion (3.3) uses a Reynolds decomposition of the velocity and vorticity fields. On the other hand, theoretical studies of the linearised vortex dynamics assume deterministic perturbations of a laminar base-state vortex. It is not *a priori* obvious that these stochastic fluctuations around the mean can be identified with deterministic perturbations of the base flow (North 1984).

We have shown above that within our leading-order approximation the mean and base flows can be identified. Assuming that the eigenmodes constitute a complete description of the linearised dynamics (Arendt, Fritts & Andreassen 1997; Fabre *et al.* 2006; Roy & Subramanian 2014), arbitrary fluctuations can be represented as linear combinations of these eigenmodes. The meandering postulate (3.6) implies that the fluctuation vorticity associated with meandering must be dipolar. On the other hand, Bölle (2023) demonstrated theoretically that the vortex-centre positions X_α are directly related to the leading two POD modes $\hat{\phi}^{(\alpha)}$ of the vorticity field, which exhibit a similar dipolar pattern (see figure 10). Ample experimental evidence for this X_α–$\hat{\phi}^{(\alpha)}$ correspondence can be found in the literature (Edstrand *et al.* 2016; Karami *et al.* 2019; Bölle *et al.* 2023). However, agreement between the leading POD mode patterns and fluctuations predicted by the meandering postulate has not been shown before. Therefore, in order to check the appropriateness of our hypotheses, figure 7(*b*) displays the vorticity fluctuation leading to a vortex displacement, computed for a Gaussian vortex. For small displacements, this is well represented by the first-order approximation (3.11) used here. Both are qualitatively

and quantitatively similar to the leading POD mode, which we know is associated with meandering.

As already recognised before (Jacquin *et al.* 2001; Edstrand *et al.* 2016), the fluctuation shown in figures 7(*b*) and 10 is well represented by a displacement (D) Kelvin eigenmode of linear vortex dynamics (Fabre *et al.* 2006; Bölle *et al.* 2021). This suggests that vortex meandering is due to surrounding turbulence exciting an infinity of displacement Kelvin waves propagating along the vortex (Melander & Hussain 1993; Marshall & Beninati 2005; Pradeep & Hussain 2010). Displacement-like perturbations are found very generically as the most energetic vortex-response modes (e.g. Gutierrez-Castillo *et al.* 2022; Bölle *et al.* 2023; Garrido-Martin *et al.* 2025). We therefore propose to identify ω_v and the corresponding ς_s in § 3.3 with the theoretical relations of displacement vortex eigenmodes. We determined the dispersion relation of the D mode of the vortex in our experiment, using the procedure given by Fabre & Jacquin (2004) and the analytical expression (2.3) for the swirl velocity profile. The result for the frequency $\omega_{1,0}$ can with good accuracy be expressed in the form proposed by Fabre (2002), which has the correct asymptotic behaviour:

$$\frac{\omega_{1,0}}{\Omega_0}(kr_c) = -\frac{(kr_c)^2}{2 + C_1|k|r_c + C_2(kr_c)^2}\left[\ln\left(\frac{2 + C_3|k|r_c}{|k|r_c}\right) + \frac{1}{4} - \gamma\right], \tag{3.22}$$

with $C_1 = 2.6742$, $C_2 = 0.7613$, $C_3 = 2.9698$, Euler's constant $\gamma = 0.5772\ldots$ and k the axial wavenumber. The ratio between core radius r_c and the parameter a in (2.3) depends on the value of n and is $r_c/a \approx 1.30$ in the present case.

The D modes are neutrally stable to leading order (in Reynolds number) and regularly perturbed by viscosity. For our experimental vortex, we therefore consider a damping rate given to a good approximation by νk^2, in agreement with Fabre (2002). Together with (3.22), this yields the viscous dispersion relation of the D mode

$$\frac{\omega_{\mathrm{D}}(kr_c)}{\Omega_0} = \frac{\omega_{1,0}(kr_c)}{\Omega_0} + \mathrm{i}\frac{(kr_c)^2}{Re_c}, \tag{3.23}$$

where $Re_c = \Omega_0 {r_c}^2/\nu$ is the core Reynolds number. According to (3.13), all vortex eigenmodes are subject to advection by the free stream flow, for which the dispersion relation (for a fixed measurement position) reads

$$\frac{\omega_a(kr_c)}{\Omega_0} = -\frac{U_0}{r_c\Omega_0}kr_c. \tag{3.24}$$

Adding (3.23) and (3.24) yields the dispersion relation for the advected D modes

$$D[\omega, k; \nu] = \frac{\omega_{1,0}(kr_c)}{\Omega_0} - \frac{U_0}{r_c\Omega_0}kr_c + \mathrm{i}\frac{(kr_c)^2}{Re_c} = 0. \tag{3.25}$$

The real part of (3.25),

$$\frac{\omega(kr_c)}{\Omega_0} = \frac{\omega_{1,0}(kr_c)}{\Omega_0} - \frac{U_0}{r_c\Omega_0}kr_c \quad \overset{kr_c \gg 1}{\longrightarrow} \quad \frac{\omega(kr_c)}{\Omega_0} = -1 - \frac{U_0}{r_c\Omega_0}kr_c \tag{3.26}$$

corresponding to the inviscid dispersion relation, describes the frequency shift of the D modes due to advection (figure 8). Damping occurs mainly for non-zero wavenumbers of the order of $kr_c \sim 1$ or larger. The frequency $\omega_{1,0}$ of the D mode in (3.22) asymptotes to $\omega_{1,0}/\Omega_0 \to -1$ as $kr_c \to \infty$ (see also Fabre 2002). This yields the second equality in (3.26), valid for $kr_c \gg 1$. In this limit of short wavelengths, we can invert (3.26) to obtain

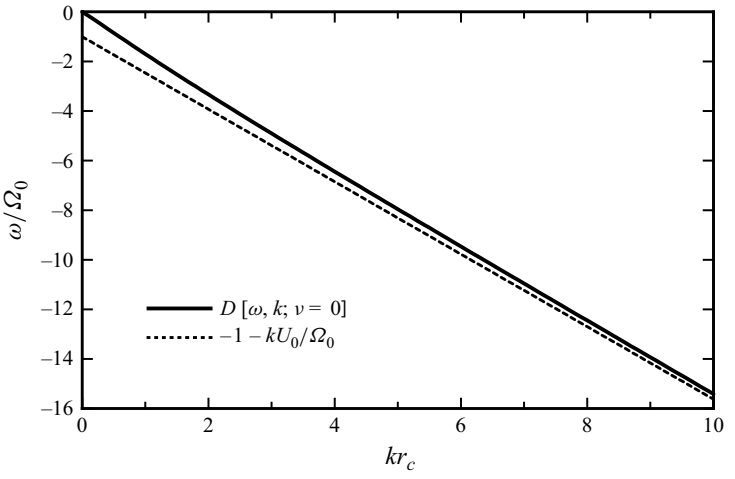


Figure 8. Inviscid dispersion relation for the displacement (D) mode of the experimental vortex subject to advection at U_0. The frequency $\omega(k)$ is asymptotically due to advection (3.26), dominating for wavelengths shorter than r_c.

$kr_c = (\Omega_0 - \omega)r_c/U_0$. Inserting this into the imaginary part of the dispersion relation (3.25) yields the temporal spectral damping

$$\frac{\varsigma(\omega)}{\Omega_0} = \frac{1}{Re_c}\left(1 - \frac{\omega}{\Omega_0}\right)^2 \left(\frac{r_c\Omega_0}{U_0}\right)^2 \quad (kr_c \gg 1) \tag{3.27}$$

as a function of ω only, which is experimentally measurable. For the particular case of D modes considered here, we then deduce the spatial spectral damping rate

$$\varsigma_s(\omega)r_c = \frac{\varsigma(\omega)}{\Omega_0}\frac{r_c\Omega_0}{U_0} = \frac{1}{Re_c}\left(1 - \frac{\omega}{\Omega_0}\right)^2 \left(\frac{r_c\Omega_0}{U_0}\right)^3 \quad (kr_c \gg 1). \tag{3.28}$$

From (3.26) follows the group velocity $U_0/r_c\Omega_0$ for $kr_c \gg 0$, such that the above transformation (3.28) from temporal to spatial damping rates corresponds to Gaster's transform. Finally, inserting the spatial damping (3.28) for the D mode into (3.21), we obtain

$$\overline{|\hat{X}'_\alpha|^2}(z, \omega) = \frac{DU_0}{\nu}\frac{1}{(\Omega_0 - \omega)^2}\left[1 - e^{-2\frac{\nu(\Omega_0-\omega)^2}{U_0^3}z}\right]. \tag{3.29}$$

Bölle (2021, 2023) proposed that meandering essentially corresponds to a Brownian motion of the vortex and can be described adequately by an Ornstein–Uhlenbeck process. The PSD in this case is given by (Yaglom 1962)

$$S(z, \omega) = \frac{\sigma^2(z)}{\pi}\frac{\lambda}{\omega^2 + \lambda^2}, \tag{3.30}$$

where λ denotes the reciprocal response (damping) time scale of the vortex (Brownian particle). Equation (3.30) was shown to provide a very good fit to experimentally measured spectra of the vortex displacement (Bölle 2024). Whereas an Ornstein–Uhlenbeck process is characterised by a single response time scale λ^{-1}, our model has an infinity of time scales associated with the spectral damping, i.e. the viscous damping of the regular vortex eigenmodes at finite Reynolds numbers.

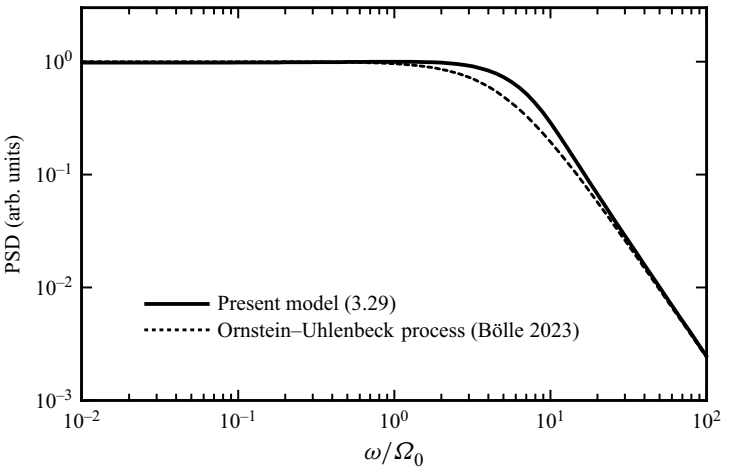


Figure 9. The PSD of vortex meandering motion: comparison between the prediction (3.29) of the present model, using experimental parameter values, and the PSD of an Ornstein–Uhlenbeck process (3.30), where the reciprocal time scale λ is set according to (3.33).

Matching the asymptotic behaviour of (3.29) and (3.30), one can obtain a relationship between the fluid viscosity ν appearing in our model and the decay rate λ. In particular, we consider the limit as $\omega \to 0$ and $0 \ll \omega \ll \infty$. We therefore require that

$$\overline{|\hat{X}'_\alpha|^2}(z,0) = \frac{2Dz}{U_0^2} \overset{!}{=} \frac{\sigma^2}{\pi}\frac{1}{\lambda} = S(z,0) \qquad (\omega \to 0), \tag{3.31}$$

$$\overline{|\hat{X}'_\alpha|^2}(z,\omega) = \frac{DU_0}{\nu\omega^2} \overset{!}{=} \frac{\sigma^2}{\pi}\frac{\lambda}{\omega^2} = S(z,\omega) \qquad (0 \ll \omega \ll \infty). \tag{3.32}$$

Taking the limit as $\omega \to \infty$, we see from (3.32) that the spectral energy vanishes for infinitely large frequencies. Solving (3.32) for D, inserting into (3.31) and solving for λ yields

$$\lambda = \sqrt{\frac{U_0^3}{2\nu z}}. \tag{3.33}$$

Evaluating (3.33) for the present experiment (§ 2), *viz.* $U_0 = 79.1\,\mathrm{cm\,s^{-1}}$, $\nu = 1 \times 10^{-2}\,\mathrm{cm\,s^{-2}}$ and $z = 110\,\mathrm{cm}$, yields $\lambda = 474\,\mathrm{s^{-1}}$. Figure 9 displays a comparison between (3.29) and (3.30), using the above scaling, showing that the spectrum predicted from the present model closely resembles the one of an Ornstein–Uhlenbeck process. We show in § 4.3 below that a suitable value for λ, from a fit to the experimental data, would rather be $\lambda \approx 2\,\mathrm{s^{-1}}$, which is two orders of magnitude smaller than the one inferred from the present model based on the viscous decay of vortex Kelvin modes.

4. Validation of meandering model from experiment

In § 3.2, we have shown that the integrals in the meandering model (3.5) (derived in § 3.1) mutually compensate in a leading-order approximation. In the following, we corroborate this result for the given experiment. Recalling from § 2 that our PIV measurement set-up only allows us to determine the in-plane components of velocity and the streamwise vorticity, a direct experimental evaluation of the model integrals is possible only for the first line of (3.5).

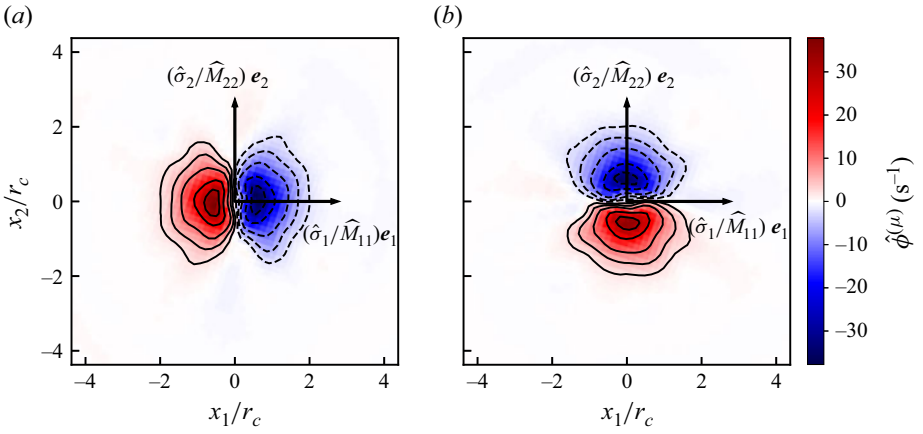


Figure 10. Estimates of the (*a*) first and (*b*) second vorticity POD modes in the vortex-centre principal-axes system, with positive (negative) values corresponding to red (blue) colour shading and solid (dashed) contours. The axes $\boldsymbol{e}_\alpha$ are scaled by the corresponding meandering amplitudes $\hat{\sigma}_\alpha$ and transformed to the POD system by $\widehat{M}^{-1}_{\alpha\alpha}$ (see § 4.2).

4.1. *Proper orthogonal decomposition*

A simplification of (3.5) is possible by expansion of the rotational fluctuation fields w'_z and u'_α in the leading modes of a POD, as discussed in § 3.4. The expansion of the fluctuation vorticity in POD modes reads (Holmes, Lumley & Berkooz 1996)

$$w'_z(\boldsymbol{x}, z, t) = \sum_{\mu=1}^{\infty} a_\mu(z, t)\phi^{(\mu)}(\boldsymbol{x}), \tag{4.1}$$

$$\text{such that} \quad (\phi^{(\mu)}, \phi^{(\nu)}) = \sigma_\mu^2 \delta_{\mu\nu} \quad \text{and} \quad \overline{a_\mu a_\nu} = \delta_{\mu\nu} \quad \forall \mu, \nu. \tag{4.2}$$

Contrary to our general convention, Greek indices in the POD, for now, run through all positive integer values, which we express by writing the sums explicitly. As usual, $(\cdot, \cdot)$ denotes the $L^2(M)$-inner product and $||\cdot||$ the induced norm (Holmes *et al.* 1996). The corresponding rotational fluctuation-velocity modes are then obtained from the relevant Biot–Savart integrals (Saffman 1995)

$$\psi_1^{(\mu)}(\boldsymbol{x}) = -\frac{1}{2\pi}\int_M \mathrm{d}^2x'\,\phi^{(\mu)}(\boldsymbol{x}')\frac{x_2 - x'_2}{|\boldsymbol{x} - \boldsymbol{x}'|^2} \quad \text{and} \tag{4.3}$$

$$\psi_2^{(\mu)}(\boldsymbol{x}) = \frac{1}{2\pi}\int_M \mathrm{d}^2x'\,\phi^{(\mu)}(\boldsymbol{x}')\frac{x_1 - x'_1}{|\boldsymbol{x} - \boldsymbol{x}'|^2}, \tag{4.4}$$

where $|\cdot|$ denotes the Euclidean vector norm in the measurement plane (cf. § 3.2).

Figure 10 shows estimators $\hat{\phi}^{(\mu)}$ of the true vorticity POD modes $\phi^{(\mu)}$, $\mu = 1, 2$, for the given experiment (Bölle 2024). Using standard notation, statistical estimators are indicated by a circumflex in the following (see § 4.3). Superposition of the (scaled) principal axes illustrates their alignment with the leading POD modes. This alignment, together with the characteristic dipolar spatial pattern, yields the proportionality of the visually manifest meandering motion X_μ and the leading-order dynamic vorticity fluctuation a_μ (Bölle 2023, 2024). Figure 11 confirms that the $X_\mu(t)$ and $a_\mu(t)$ time series, when scaled according to our derivation in § 4.2, indeed overlap.

Figure 12 shows the rotational fluctuation velocity estimates $\hat{\psi}_\alpha^{(\mu)}$ along the vortex-centre principal axes, computed by numerically solving (4.3) and (4.4). As assumed in the

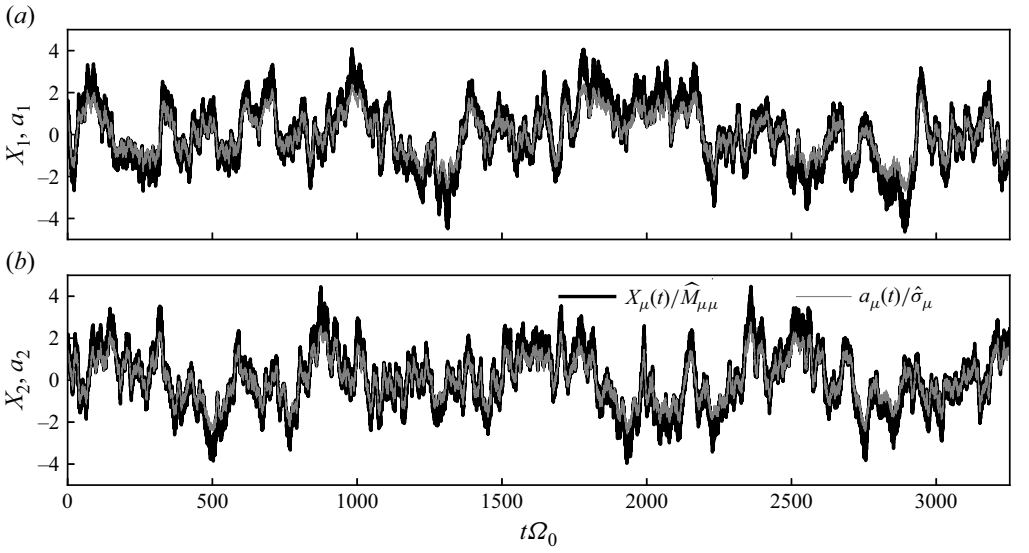


Figure 11. Comparison of the observed vortex deflection X_μ (figure 5) with the time series of the amplitudes of the (*a*) first and (*b*) second vorticity POD modes. When appropriately scaled by $\widehat{M}_{\mu\mu}$ (see (4.7)) and $\hat{\sigma}_\mu$, respectively, the time series overlap.

model derivation (§ 3.1), the leading vortex-response modes shown in figures 10 and 12 have essentially a compact support in M. We note that the Biot–Savart velocities of the leading vorticity POD modes shown in figure 12 are practically identical – qualitatively and quantitatively – to the leading velocity POD modes (not shown).

4.2. *Numerical evaluation of the model integrals*

Injecting the expansions of the fluctuation vorticity and rotational velocity in their respective modes (4.1)–(4.4) into the first line of (3.5) yields

$$\sum_{\mu=1}^{\infty}\left[\frac{1}{\Gamma}\int_M \mathrm{d}^2x\, x_\alpha \phi^{(\mu)}\right]\frac{\mathrm{d}a_\mu}{\mathrm{d}t} = \sum_{\mu=1}^{\infty}\left[\frac{1}{\Gamma}\int_M \mathrm{d}^2x\, \overline{u}_\alpha \phi^{(\mu)}\right] a_\mu + \sum_{\mu=1}^{\infty}\left[\frac{1}{\Gamma}\int_M \mathrm{d}^2x\, \overline{w}_z \psi_\alpha^{(\mu)}\right] a_\mu + \left[\frac{1}{\Gamma}\int_M \mathrm{d}^2x\, \overline{w}_z U'_\alpha(t,\boldsymbol{x})\right] + \xi_\alpha(t) \quad (\alpha = 1, 2). \tag{4.5}$$

For further simplification, we use the fact that the vortex-meandering motion is essentially determined by the leading two POD modes (Bölle 2023). Hence, we can truncate the POD expansion to $\mu = 1, 2$ in the following and express (4.5) in the symbolic matrix-vector form:

$$\boldsymbol{M}\left(\frac{\partial \boldsymbol{a}}{\partial t} + U_0\frac{\partial \boldsymbol{a}}{\partial z}\right) = \boldsymbol{K}\boldsymbol{a} + \boldsymbol{\eta}(t) + \boldsymbol{\xi}(t). \tag{4.6}$$

The entries of matrices $\boldsymbol{M}$ and $\boldsymbol{K}$ correspond to the left-hand side and right-hand side integrals of the first line of (4.5), respectively. Here $\boldsymbol{K}$ includes contributions from advection by the mean velocity and from stretching by the mean vorticity. The integrals of the second line of (4.5) involving the (given) fluctuating potential flow correspond to an external forcing $\boldsymbol{\eta}(t)$.

The principal structure and order-of-magnitude values of the matrices $\boldsymbol{M}$ and $\boldsymbol{K}$ can be deduced from the characteristic symmetries and scales of the flow fields. Figures 10

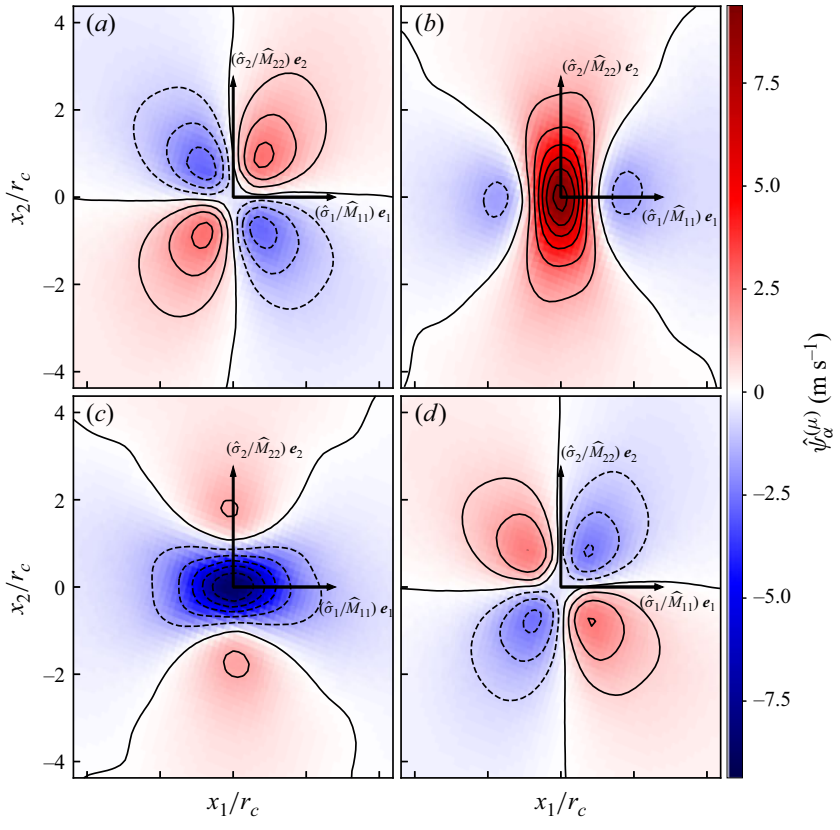


Figure 12. Rotational fluctuation velocities associated with the leading vorticity POD modes in the x_1–x_2 system, computed from Biot–Savart integrals: (*a*) $\hat{\psi}_1^{(1)}$, (*b*) $\hat{\psi}_2^{(1)}$, (*c*) $\hat{\psi}_1^{(2)}$, (*d*) $\hat{\psi}_2^{(2)}$. The vortex-centre principal axes $\boldsymbol{e}_\alpha$, scaled by the corresponding meandering amplitudes $\hat{\sigma}_\alpha$ and transformed to POD system by $\widehat{M}_{\alpha\alpha}^{-1}$, are shown as arrows.

and 12 suggest that $\ell \sim r_c \sim 0.5$ cm is a reasonable length scale estimate over which vorticity and velocity fluctuations associated with vortex meandering change appreciably. The same length scale characterises the mean flow (figure 6). The integration domain's lateral dimension is $O(10\ell)$ and therefore roughly an order of magnitude larger than the characteristic spatial variability. Figure 10 further suggests to take the maximum $\omega' \sim 30\ \mathrm{s}^{-1}$ as the characteristic scale for the vorticity fluctuations. With the Biot–Savart law (4.3)–(4.4), we deduce the corresponding velocity scale $u' \sim (2\pi)^{-1}\ell\omega' \sim 3\ \mathrm{cm\ s}^{-1}$ (cf. also figure 12). Finally, characteristic scales of the mean vorticity and velocity are $\bar{\omega} \sim \Omega_0 \sim 100\ \mathrm{s}^{-1}$ and $\bar{u} \sim 0.6 \times r_c\Omega_0 \sim 30\ \mathrm{cm\ s}^{-1}$ (figure 6). The matrix structure is deduced from the typical spatial symmetries of the mean fields and POD modes in the principal axes system. For guidance, estimates of the leading vorticity POD modes $\hat{\phi}^{(\mu)}$ and their corresponding velocities $\hat{\psi}_\alpha^{(\mu)}$ (α, $\mu = 1, 2$) computed from the given experiment are shown in figures 10 and 12. Inspection of the characteristic dipolar vorticity pattern of $\hat{\phi}^{(\mu)}$ in figure 10 readily reveals that

$$M_{\alpha\mu} = \frac{1}{\Gamma}\int_M \mathrm{d}^2x\, x_\alpha \phi^{(\mu)} \sim \frac{\ell\omega'}{\bar{\omega}}\delta_{\alpha\mu} \sim 0.1\ \mathrm{cm}\,\delta_{\alpha\mu}, \tag{4.7}$$

because of the linear weighting with the principal coordinates. The direct proportionality between the experimentally visible vortex meandering X_μ and the evolution in the

phase space spanned by the leading POD modes a_μ expressed by (4.7) was termed kinematic-dynamic equivalence (Bölle 2023).

Analogously, the contribution to $\boldsymbol{K}$ from advection by the mean velocity is

$$K^A_{\alpha\mu} = \frac{1}{\Gamma}\int_M \mathrm{d}^2x\, \overline{u}_\alpha \phi^{(\mu)} \sim \frac{\bar{u}w'}{\bar{w}}\varepsilon_{\alpha\mu} \sim 3\ \mathrm{cm\ s^{-1}}\ \varepsilon_{\alpha\mu}, \tag{4.8}$$

where $\varepsilon_{\alpha\mu}$ denotes the two-dimensional Levi–Civita symbol (symbolically, $\boldsymbol{E} = -\boldsymbol{E}^{\mathrm{T}}$). Equation (4.8) expresses the fact that transport due to advection corresponds to a skew-symmetric matrix and is hence a conservation principle. In the present case of a line vortex, (4.8) corresponds to conserved circular advection in the measurement plane by the vortex mean flow.

From figure 12, we infer that the velocity modes $\psi^{(\mu)}_\alpha$ in (4.9) should be structurally similar and, moreover, that $\operatorname{sgn}\psi^{(1)}_1 = -\operatorname{sgn}\psi^{(2)}_2$ and $\operatorname{sgn}\psi^{(2)}_1 = -\operatorname{sgn}\psi^{(1)}_2$, where sgn denotes the sign function. The orientation in the plane is irrelevant for the integrals in (4.9), since the mean streamwise vorticity is essentially rotationally symmetric and, hence, contributes the same weight along all directions. The integrals should therefore yield comparable contributions in magnitude and we thus obtain the estimate

$$K^S_{\alpha\mu} = \frac{1}{\Gamma}\int_M \mathrm{d}^2x\, \overline{w}_z \psi^{(\mu)}_\alpha \sim u'\varepsilon_{\alpha\mu} \sim 3\ \mathrm{cm\ s^{-1}}\ \varepsilon_{\alpha\mu} \tag{4.9}$$

for the contribution to $\boldsymbol{K}$ from stretching by the mean vorticity.

To check our estimation of the matrices $\boldsymbol{M}$ and $\boldsymbol{K}$ in § 3, we solve (4.7)–(4.9) numerically for the given experiment using the trapezoidal rule,

$$\widehat{\boldsymbol{M}} = \begin{bmatrix} 0.080\ \mathrm{cm} & -0.001\ \mathrm{cm} \\ 0.004\ \mathrm{cm} & 0.080\ \mathrm{cm} \end{bmatrix} \sim \begin{bmatrix} 10^{-1} & 0 \\ 0 & 10^{-1} \end{bmatrix} \mathrm{cm}, \tag{4.10}$$

$$\widehat{\boldsymbol{K}}^A = \begin{bmatrix} 0.230\ \mathrm{cm\ s^{-1}} & 2.830\ \mathrm{cm\ s^{-1}} \\ -3.042\ \mathrm{cm\ s^{-1}} & 0.164\ \mathrm{cm\ s^{-1}} \end{bmatrix} \sim \begin{bmatrix} 0 & 1 \\ -1 & 0 \end{bmatrix} \mathrm{cm\ s^{-1}}, \tag{4.11}$$

$$\widehat{\boldsymbol{K}}^S = \begin{bmatrix} -0.160\ \mathrm{cm\ s^{-1}} & -2.740\ \mathrm{cm\ s^{-1}} \\ 2.930\ \mathrm{cm\ s^{-1}} & -0.120\ \mathrm{cm\ s^{-1}} \end{bmatrix} \sim \begin{bmatrix} 0 & -1 \\ 1 & 0 \end{bmatrix} \mathrm{cm\ s^{-1}}, \tag{4.12}$$

which is consistent with the estimations given in (4.7)–(4.9). The numerically inverted $\widehat{\boldsymbol{M}}^{-1}$ is used in figure 11 for scaling. In agreement with our theoretical prediction in § 3.2, $\widehat{\boldsymbol{K}}^A$ and $\widehat{\boldsymbol{K}}^S$ mutually cancel to good approximation and $\widehat{\boldsymbol{K}} \approx 0$.

4.3. *Comparison of model characteristics with experiment*

In what follows, we consider the principal-component time series $a_\mu(t)$ $(\mu = 1, 2)$ corresponding to the leading expansion coefficients in a POD development of the streamwise fluctuation vorticity (cf. (4.1), setting $z = z_M = \mathrm{const}$). This is a bivariate, stationary, centred random process. However, experimentally available are only finite samples $\{a_\mu(n)\}$, $n = 1, 2, \ldots, N$, consisting of autocorrelated, identically distributed realisations probed at constant Δt. We emphasise that we can only compute estimators of the actual statistical characteristics for the given finite samples (for a discussion of statistical inference in the context of vortex meandering, see Bölle (2024)).

A priori we do not know the population probability distribution of a_μ. Therefore, in order to estimate the uncertainty of the sample statistical characteristics computed from one experimental sample, we use moving-block bootstrapping to account for serial correlation in the data (Wilks 1997; von Storch & Zwiers 2003; Wilks 2006). Our analysis in § 3 suggests that the vortex-response dynamics is characterised by two time scales t_v

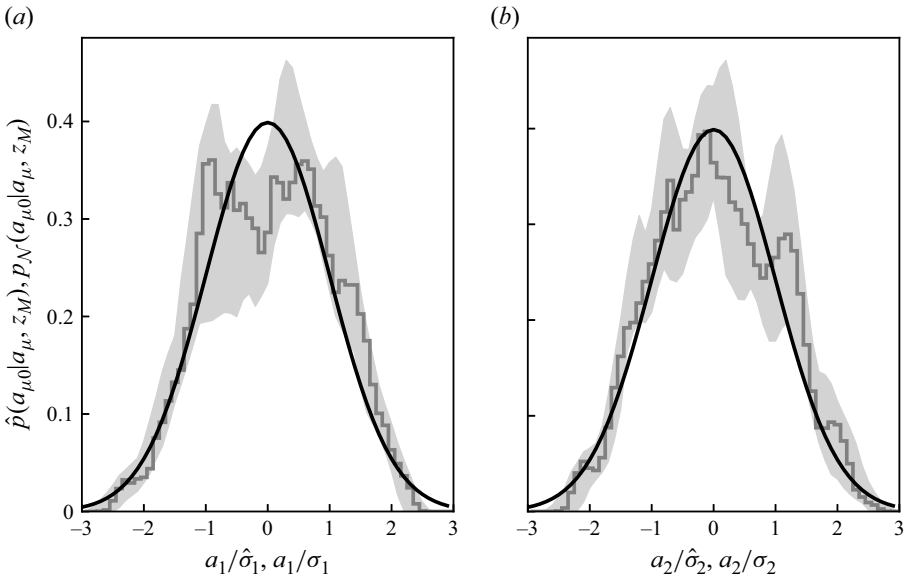


Figure 13. Frequency distribution $\hat{p}(a_{\mu 0}|a_\mu, z_M)$ histograms of the normalised (*a*) first and (*b*) second principal-component time series assuming 60 bins (grey solid line). Grey shading indicates the 95 % confidence interval computed from $N_b = 10^3$ moving-block bootstrap samples. The solid black lines displays the probability density of a standard normal distribution.

and t_w. For second-order autoregressive processes the block length L can be estimated from the implicit formula (Wilks 1997, 2006)

$$L = (N - L + 1)^{\frac{2}{3} - \frac{1}{3}\sqrt{\frac{N'}{N}} e^{-3/2N}}, \tag{4.13}$$

where N' denotes the effective sample size (Bölle 2024). Numerically solving (4.13) by bisection yields $L = 1005$, which is approximately twice the intrinsic response time scale $2t_v/\Delta t$ over which time series are correlated. However, using this block length does not reproduce the correlation structure associated with the low-frequency periodic dynamics, since the periodic time scale t_w induced by the free-surface potential flow is approximately an order of magnitude larger than the intrinsic relaxation scale t_r, *viz.* $t_w/t_v \sim 10$. This suggests to take the block length L of the order of $t_w/\Delta t$. Specifically setting $L = 12752$, such that the sample of length N is covered by exactly $b = 3$ contiguous blocks, yields plausible results and will be used henceforth. For the bootstrapping, we draw with uniform probability from the original sample with replacement. Repeating this procedure N_b times, we construct a set of $N_b = 10^3$ samples that could have been realised instead of the one actually measured. For $\tilde{p} \in (0, 1)$, the $(1 \pm \tilde{p})/2$ percentiles then define the $\tilde{p} \times 100\%$ confidence interval (von Storch & Zwiers 2003; Wilks 2006).

We define the sample variance $\hat{\sigma}_\mu^2 = (1/N)\sum_{n=1}^{N} a_\mu^2(n)$, which is the maximum likelihood estimator if the a_μ are normally distributed. For the present experiment, the point estimator and 95 % confidence interval of the standard deviation are $\hat{\sigma}_1/\Omega_0 = 2.81 \pm 0.02$, $\hat{\sigma}_2/\Omega_0 = 2.62 \pm 0.02$. Normalising a_μ with these point estimators, figure 13 shows the frequency distribution of the first two principal-component time series $\hat{p}(a_{\mu 0}|a_\mu, z_M)$ along with the 95 % confidence intervals obtained from moving-block bootstrapping. The frequency distribution and the 95 % confidence intervals coincide reasonably well with a standard normal distribution (figure 13). This is a well-known finding in

vortex-meandering experiments (Bailey & Tavoularis 2008; Dghim *et al.* 2021; Bölle 2024), although the agreement is somewhat less good than reported previously.

We recall that a perfect Brownian motion-like dynamics would be associated with a normal distribution (Bölle 2023), while a perfectly periodic fluctuation would have a U-shaped probability density with maxima at the oscillation amplitudes (Tennekes & Lumley 1972). This periodicity exerted by the free-surface wave may be visible in the two peaks around $a_\mu \hat{\sigma}_\mu^{-1} \sim \pm 1$. The fact that this double-peak structure is apparent also in the 95 % confidence interval suggests that it is a reproducible statistical characteristic.

Neglecting the influence of the free surface, we have shown in § 3.3 that our model power spectrum qualitatively corresponds to that of an Ornstein–Uhlenbeck process describing Brownian motion. From (3.30), we obtain,

$$\lambda_\mu \frac{\pi S_{\mu\mu}(\omega)}{\sigma^2} = \frac{\lambda_\mu^2}{\lambda_\mu^2 + \omega^2} \overset{\omega \to 0}{\to} 1 \quad (\mu = 1, 2 \text{ not summed}). \tag{4.14}$$

Due to linearity, periodic components with a specific frequency Ω and amplitude A_w correspond to Dirac-localised peaks $A_w^2 \delta(\omega - \Omega)$ superposed to (4.14). It would be expected that any dynamically important periodicity should manifest as a reproducible and statistically significant peak in the sample power spectra. For the normalisation of the sample power spectra $\hat{G}_{\mu\mu}(\omega)$, we use that $G_{\mu\mu}(\omega = 0)\sigma_\mu^{-2} = 2t_\mu$ by the Wiener–Khinchin theorem, whereas $t_\mu = \lambda_\mu^{-1}$ denotes the integral time scales (Yaglom 1962; Bölle 2024). Hence,

$$\lambda_\mu \frac{G_{\mu\mu}(\omega)}{2\sigma_\mu^2} \overset{\omega \to 0}{\to} 1 \quad (\mu = 1, 2 \text{ not summed}). \tag{4.15}$$

Figure 14 shows a comparison of the normalised sample power spectra (4.15) with the normalised Ornstein–Uhlenbeck process spectra (4.14). The model fits the sample spectra remarkably well and is essentially contained in the 95 % confidence interval computed from the $N_b = 10^3$ moving-block bootstrap sample. Consequently, for the present experiment, we cannot reject (and hence would accept) the null hypothesis that vortex meandering corresponds to an Ornstein–Uhlenbeck process at the 5 % level of significance (Bölle 2023, 2024). The sample power spectra are normalised by using the respective point estimators in (4.15), where we estimate $\hat{\lambda}_\mu$ from an exponential fit to the sample correlation functions (see below). It is well known that this yields more robust estimators than inferring them from the sample spectra directly (von Storch & Zwiers 2003). It should be stressed that the thus obtained Brownian-motion (reciprocal) response time scale $\hat{\lambda}_\mu \Omega_0^{-1} \approx 0.02$ (or equivalently $t_\mu \Omega_0 \approx 50$) is approximately two orders of magnitude smaller than our theoretical estimate of $\lambda_\mu \Omega_0^{-1} \approx 5.00$ (§ 3.4). This should be contrasted with the overall very good quantitative agreement between (4.14) and (4.15) in figure 14. Finally, we note that there is no clearly discernible peak around the wave period $\Omega \Omega_0^{-1} \sim 0.007$ (see § 5.1) in the sample power spectra that would be reproducible and statistically significant (figure 14).

5. Effect of surface gravity waves

In this section, we examine the combined effect of residual, small-scale turbulence and free-surface gravity waves on vortex meandering. We recall that our model of vortex meandering, *viz.* the excitation of an infinity of damped Kelvin waves propagating along

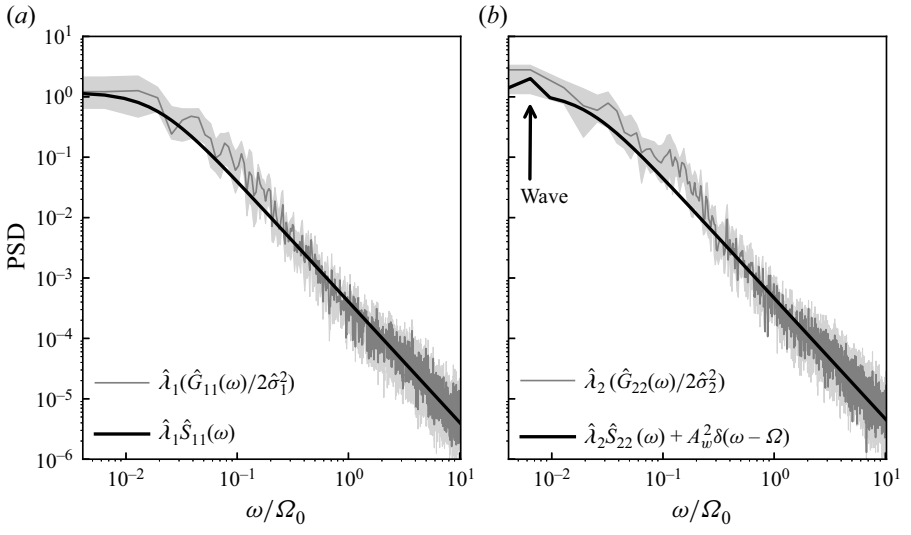


Figure 14. Non-dimensional sample PSD of the (*a*) first and (*b*) second principal-component time series (grey thin line). Grey shading indicates the 95 % confidence interval computed from the $N_b = 10^3$ moving-block bootstrap sample. Superposed are the normalised power spectra (4.14) of an Ornstein–Uhlenbeck process (black thick line), with an additional peak (indicated by an arrow) at the frequency of the gravity wave in the water channel for the vertical vortex displacement in (*b*).

the core, is associated with a spectral damping as a function of frequency. However, our analyses suggest that it is possible to associate vortex meandering with the single characteristic response time scales $t_\mu = \lambda_\mu^{-1}$. Assuming $a_\mu(t)$ to be uncoupled (Bölle (2024) shows that they are uncorrelated in another experiment) and the existence of single characteristic time scales, the equation of motion in terms of the leading POD expansion coefficients reads

$$\frac{\mathrm{d}a_\mu}{\mathrm{d}t} = \lambda_\mu a_\mu + \eta_\mu(t) + \xi_\mu(t) \quad (\mu = 1, 2 \text{ not summed}). \tag{5.1}$$

5.1. *Forcing from a plane surface gravity wave*

In § 2, we provided evidence that in the present experiment the vortex dynamics is subject to potential-flow forcing exerted by gravity waves forming on the free surface of the water channel, with a frequency given by (2.1). We recall from § 2 that the water-channel depth is $d = 45$ cm and that the mean vortex-centre position is at $h_v \approx 16$ cm above the channel floor. The measured wave frequency is $f_s = 0.11$ Hz.

The (two-dimensional) wave velocity field in the channel-fixed coordinate system (figure 4*a*) reads (Landau & Lifshitz 1987)

$$U_z'(y, z, t) = -A\cosh(k(h_v + y))\sin(kz - \Omega t) = -A_z(y)\sin(kz - \Omega t), \tag{5.2}$$

$$U_y'(y, z, t) = A\sinh(k(h_v + y))\cos(kz - \Omega t) = A_y(y)\sin(kz - \Omega t), \tag{5.3}$$

where A is the amplitude, and $\Omega = 2\pi f_s$ and $k = \pi/L$ denote the angular frequency and wavenumber, respectively (L is the equivalent channel length compatible with the sloshing dynamics, see § 2.2). The amplitudes A_z and A_y of the streamwise and vertical velocity oscillations are related through (2.2). The amplitude at the location of the vortex can be estimated from the time series in figure 2(*a*) and the spectral content of the sloshing

peak in figure 3(*a*) as $A_z(y=0) \approx 1.0\,\mathrm{cm\,s^{-1}}$. Since $h_v \ll L$, relation (2.2) then yields $A_y(y=0) \approx \pi A_z h_v/L \approx 0.07\,\mathrm{cm\,s^{-1}}$, in agreement with the observation in figure 2(*b*).

As already emphasised above, for the present experiment, we can evaluate only the forcing due to the vertical component of the wave velocity in the vortex-centre equation of motion (4.5). Hence, with $U_x' = 0$ for the gravity wave considered here, the forcing exerted by the potential flow on the vortex becomes

$$\eta_1(t) = \frac{1}{\Gamma}\int_M \mathrm{d}^2x\, \overline{w}_z U_x'(y,z,t) = 0, \tag{5.4}$$

$$\eta_2(t) = \frac{1}{\Gamma}\int_M \mathrm{d}^2x\, \overline{w}_z U_y'(y,z,t). \tag{5.5}$$

Herein, for simplicity, we have used that the x–y and x_1–x_2 coordinate systems are approximately aligned (figure 4). Considering further that for the given integration domain M, the vertical coordinate varies in the small range $\Delta y \approx \pm 3\,\mathrm{cm} \approx \pm 5 r_c$, the wave amplitude is taken as constant and equal to $A_y(y=0)$ over the domain to a good approximation. This simplifies (5.5) to

$$\eta_2(t) \approx A_y(y=0)\cos\Omega t \tag{5.6}$$

for a fixed measurement plane at $z = z_M$ and omitting an arbitrary phase. The corresponding vortex deflection amplitude induced by the free-surface gravity wave is then estimated as $A_y(y=0)/\Omega$, and its standard deviation as

$$\sigma_w = \frac{A_y(y=0)}{\sqrt{2}\Omega} \approx 0.07\,\mathrm{cm} \approx 0.12 r_c, \tag{5.7}$$

which is a significant fraction of the total meandering amplitude measured in the experiment: $\sigma \approx 0.11\,\mathrm{cm} = 0.20 r_c$. In § 2.3, the amplitude of turbulence-induced meandering was estimated as $\sigma_t \approx 0.14 r_c$. The two estimates for σ_w and σ_t are of the same order in our configuration, and they add up quadratically quite well to the observed total value.

5.2. *Correlation function*

In § 4.3, we have shown that empirical power spectra are not ideal to infer significant periodicities in noisy data, since the associated peaks not necessarily separate clearly from the background noise. Rather, the combined periodic–coloured-noise behaviour shows up much better in the autocorrelation functions. Quite generally, correlation functions are expected to be an efficient means to detect 'hidden' periodicities in correlated-noise signals if the time scales are sufficiently separated and the energy contained in the periodic component is at least of the same order as the noise. In this case, noise-related correlations are limited to a short time range, while eventually the correlation due to periodicity dominates. The autocorrelation function associated with (5.1) can be computed analytically,

$$\rho_{\mu\mu}(\tau) = \overline{a_\mu(t+\tau)a_\mu(t)} = \frac{A_t}{2\lambda_\mu} e^{-\lambda_\mu|\tau|} + \frac{A_w\delta_{\mu 2}}{\lambda_\mu^2+\Omega^2}\cos\Omega\tau \quad (\mu = 1,\,2 \text{ not summed}). \tag{5.8}$$

To the best of our knowledge, this autocorrelation function of a harmonically forced Langevin equation has not been given before (details are given in Appendix A).

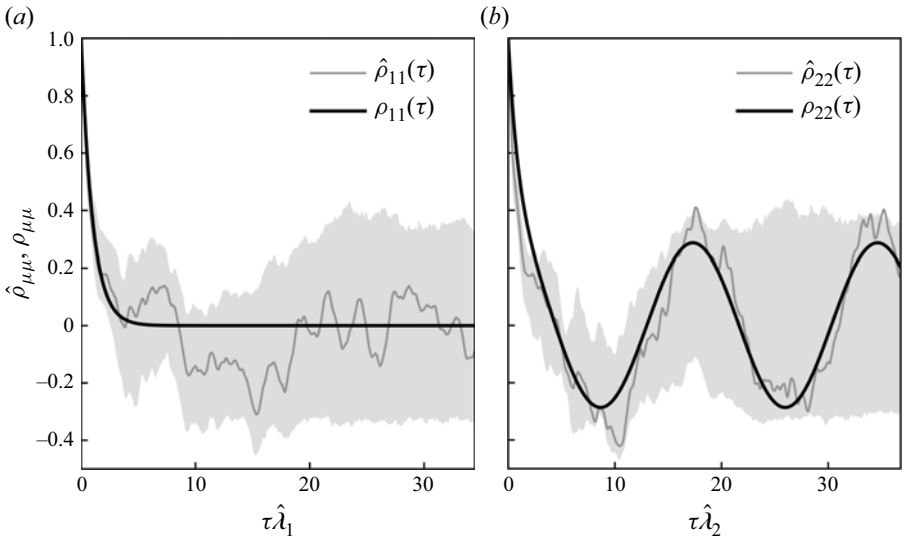


Figure 15. Comparison of the model ($\rho_{\mu\mu}$) and sample ($\hat{\rho}_{\mu\mu}$) autocorrelation functions for the (*a*) first and (*b*) second principal-component time series. The solid grey line shows the unbiased sample correlation (5.10) and light-grey shading indicates the 95 % confidence interval computed from $N_b = 10^3$ samples generated by moving-block bootstrapping. The model autocorrelation functions (5.8) are displayed as solid black lines.

Setting $\tau = 0$ in the correlation function (5.8) yields the equilibrium variance

$$\overline{a_\mu^2} = \frac{A_t}{2\lambda_\mu} + \frac{A_w}{\lambda_\mu^2 + \Omega^2} = 1, \tag{5.9}$$

due to the normalisation, which can be used to estimate A_t. We recall from § 2 that the wave period is $T_w = 9$ s and hence $\Omega = 2\pi/T_w = 0.70$ rad s^{-1}. The wave amplitude was estimated to be $A_w = 1$ s^{-2}. Taking $\hat{\lambda}_\mu \approx 2$ s^{-1} from an exponential fit of the sample correlation yields $A_t \approx 3$ s^{-1}.

We define the sample correlation functions as

$$\hat{\rho}_{\mu\gamma}(\tau) = \frac{1}{N - n_\tau} \sum_{n=1}^{N-n_\tau} \frac{a_\mu(n) a_\gamma(n + n_\tau)}{\hat{\sigma}_\mu \hat{\sigma}_\gamma}, \quad n_\tau \geq 0, \quad (\mu, \gamma = 1, 2 \text{ not summed}), \tag{5.10}$$

where $t = (n-1)\Delta t$, $\tau = n_\tau \Delta t$ and $n = 1, 2, \ldots, N$, $N = T/\Delta t$. For a stationary zero-mean process, (5.10) is an unbiased estimator. A typical alternative with less variance but higher bias would be $(N - n_\tau)N^{-1}\hat{\rho}_{\mu\gamma}(\tau)$. We found that both estimators yielded essentially the same results over the lag range τ examined (not shown).

Figure 15 shows a comparison of the sample correlations (5.10) with the model correlation functions (5.8) assuming that periodic oscillations due to the free-surface wave are induced only in the vertical coordinate. Our model correctly predicts the combined periodic–coloured-noise behaviour. Grey shading in figure 15 displays the 95 % confidence interval obtained from moving-block bootstrapping with $N_b = 10^3$. We notice that the bootstrap sample reproduces the correct correlation structure for time lags $\tau\hat{\lambda}_\mu \lesssim 20$. In particular, this shows that fluctuations in ρ_{11} for $\tau\hat{\lambda}_\mu \gtrsim 5$ are not statistically reproducible. Our model consistently stays inside the shaded area, indicating that it cannot be rejected (and hence would be accepted) at the 5 % level of significance.

6. Discussion and conclusion

6.1. *Discussion*

We summarise here the main assumptions of the proposed vortex-meandering model and discuss possible limitations. From the outset, vortex meandering is an experimental phenomenon. Therefore, we take a common but non-unique definition of vortex meandering in terms of an experimentally measurable vorticity integral (1.1) as a starting point for our model development. The idea that models of vortex meandering should start from an actually measured quantification of the phenomenon was first proposed by Bölle (2023). Given the experimentally verified spatial symmetries of the associated vorticity fields, the general vorticity integrals take leading-order approximations (3.2) accurate to within an error no larger than the third term in a POD expansion of vorticity (Bölle 2023). We then derive an equation of motion for these approximate vorticity integrals used to quantify vortex meandering in experiments, for the first time. To this end, we assume a linearised, incompressible, inviscid, three-dimensional vorticity dynamics. Ample evidence for the appropriateness of these assumptions, in particular linearity of the dynamics, is provided by previous studies (Baker *et al.* 1974; Devenport *et al.* 1996; van Jaarsveld *et al.* 2011; Bailey *et al.* 2018; Bölle 2023, 2024). Neglected terms and any externally applied excitation are accounted for by a stochastic forcing (Fontane, Brancher & Fabre 2008; Bölle *et al.* 2021). A Helmholtz decomposition of the velocity fields is used to include the effect of potential-flow perturbations on vortex meandering, in particular, the effect of free-surface gravity waves. The resulting vortex-meandering equation of motion (3.5) is then simplified by assuming that vortex meandering corresponds to a 'rigid body-like' displacement of the vortex core as a whole. This is a long-standing assumption and we refer to it as the meandering postulate (3.6) (Baker *et al.* 1974; Devenport *et al.* 1996; Bölle 2021). For the first time, we demonstrate close agreement between consequences of this postulate and experimental meandering (figure 7). Within a leading-order, linear approximation, this postulate allows us to evaluate all model integrals appearing in (3.5) exactly. We verify this result for the experimentally computable integrals in § 4.2 using a leading-order POD expansion. In essence, all model integrals mutually cancel and the final problem of vortex meandering reduces to a spatiotemporally forced, stationary advection problem (3.14)–(3.16). This problem is clearly incompatible with the characteristics of experimental meandering, most notably the intrinsic stabilisation of the dynamics associated with three-dimensional vortex eigenmodes propagating along the vortex core (Fabre *et al.* 2006; Edstrand *et al.* 2016; Bölle *et al.* 2021). Formally including the dynamics of eigenmodes, we solve the advection problem (3.14)–(3.16) assuming a stochastic forcing of the Langevin type (Fontane *et al.* 2008; Bölle 2024), which yields the exact expression (3.21) of the spectral distribution of the meandering variance at a given downstream location. In the last step, we assume that the relevant vortex eigenmodes for meandering correspond to the family of displacement (D) modes. This was speculated previously (Jacquin *et al.* 2001; Edstrand *et al.* 2016; Bölle 2021) and is consistent with the meandering postulate (3.6) for which we provided experimental evidence. Evaluating the dispersion relation (3.22) for a Moore–Saffmann vortex without axial core flow (consistent with the experiment) and including regular damping, we finally derive an estimate for the characteristic vortex-response time scale by matching our spectral solution to the known spectrum of an Ornstein–Uhlenbeck process. Agreement of vortex meandering with an Ornstein–Uhlenbeck process was demonstrated recently for another experiment (Bölle 2024) and is implied by previous studies (Baker *et al.* 1974; Devenport *et al.* 1996; van Jaarsveld *et al.* 2011). The resulting disagreement between the obtained response time and the corresponding one derived from

the experiment directly is not obvious to us. Especially, because our main assumptions are backed up against experimental evidence, as explained above. A critical point might be the impact of the neglected axial core flow, which is not available from the current experiment. However, we estimated the possible effect in the model integrals and the dispersion relation and concluded that it is probably negligible. Nevertheless, this point requires careful verification in the future. Another potentially important aspect might be the restriction to D modes. As recalled above, this decision is motivated by experimental evidence and findings of previous studies. Among the principally existing vortex eigenmodes, probably critical-layer modes would be the most obvious candidate for future study. Critical-layer modes are directly related to non-modal vortex dynamics and have been suggested to be associated with meandering (Fontane *et al.* 2008; Bölle *et al.* 2021).

6.2. *Conclusion*

Meandering is a prototype of unsteady line-vortex dynamics. Despite its ubiquitous manifestation in experiments and numerous theoretical studies, a consistent model comprising the governing mechanisms has not been proposed yet. Specifically, vortex meandering in free-surface flow subject to gravity waves has not been explicitly examined before. In this study, we develop a theoretical meandering model for a vortex evolving in a surface-wave potential flow and compare its characteristics with a respective experiment.

Meandering in experiments is identified with the vortex-centre motion in fixed mean flow-transversal measurement planes. We therefore take this definition of the vortex centre as the starting point of our model development and derive an equation of motion for it. Unlike previous studies, we use the two-dimensional vortex-centre definition as in experiments, but consider three-dimensional vorticity dynamics. This has not been reported in the literature before to the best of our knowledge. Explicitly using the postulate that meandering corresponds to lateral displacements of the vortex as a whole, we then show analytically that all measurement-plane integrals appearing in the vortex-centre equation of motion exactly cancel in a leading-order approximation. The problem of vortex meandering thus reduces to a forced advection problem in the streamwise direction. These analyses and their somewhat unexpected result have not been reported before and underscore the fundamentally three-dimensional nature of vortex-meandering dynamics. Unfortunately, streamwise gradients cannot be inferred from experiments typically conducted in transversal measurement planes. As suggested by the characteristic dipolar response-mode pattern, we therefore assume that vortex meandering corresponds to the excitation of an infinity of Kelvin displacement eigenmodes propagating along the vortex core, weakly dampened by viscosity. For this case, we can analytically solve the meandering problem and compute second-order statistics. In particular, we find the model power spectrum to be very similar to that of an Ornstein–Uhlenbeck process.

In the second part of this study, we compare the model predictions with a respective experiment conducted in a free-surface, recirculating water channel. First, computing a POD of the vorticity field, we quantitatively confirm the predicted scaling between the leading POD principal-component and vortex-centre time series. Our results extend and substantiate recent theoretical and experimental findings that these two time series are strictly equivalent. Secondly, we demonstrate that the integrals in the vortex-centre equation of motion, which we showed to cancel assuming the meandering postulate to hold, also mutually cancel for the given experiment. Finally, we compare the model-predicted second-order statistics with those estimated from the experiment. In particular, we find power-spectral approaches to be less well suited to identify hidden periodicities than correlation functions. We provide the correlation function of periodically forced Brownian motion-like dynamics, which reproduces the experimental characteristics

remarkably well. A moving-block bootstrap approach suggests that our model can be accepted at a 5 % level of significance. Nevertheless, we note that this overall very good correspondence between our model and the experiment only holds if we use the intrinsic response time scale from the experiment being approximately two orders of magnitude smaller than predicted in the model. We do not fully understand the reason for this discrepancy yet, this is the subject for further studies.

Although not entirely conclusive, we think that this study constitutes a step forward in eventually solving the problem of vortex meandering. Besides, we hope that our findings and approaches may prove useful, e.g. in marine or aeronautic applications, where vortices evolve in stratified fluids and are subject to gravity waves. Certainly, our results are pertinent for the design and interpretation of (vortex) experiments conducted in free-surface facilities.

Supplementary movies. Supplementary movies are available at https://doi.org/10.1017/jfm.2026.11698.

Acknowledgements. We would like to thank S. Le Dizès for several valuable discussions that considerably helped in the model development.

Funding. This research received no specific grant from any funding agency, commercial or not-for-profit sectors.

Declaration of interests. The authors report no conflict of interest.

Data availability statement. The data that support the findings of this study are available from the authors upon reasonable request.

Appendix A. Derivation of the autocorrelation function

Given an initial condition $\boldsymbol{a}(t_0) = \boldsymbol{a}_0$ at some initial time t_0, we can formally solve (5.1). The general solution then reads (Arnol'd 1985)

$$\boldsymbol{a}(t) - e^{t\boldsymbol{L}}\boldsymbol{a}_0 = \int_{t_0}^{t} \mathrm{d}s\, e^{(t-s)\boldsymbol{L}}[\boldsymbol{\eta}(s) + \boldsymbol{\xi}(s)]. \tag{A1}$$

The stationary state realised in the experiment formally corresponds to setting $t_0 \to -\infty$, i.e. an experiment that was started in the infinite past (Yaglom 1962). In practice, given the characteristic time scale t of the dynamics, stationarity is reached approximately for $|t_0|/t \gg 1$. For asymptotically stable dynamics, the homogeneous solution in (A1) vanishes under this condition and the vortex is in equilibrium with its environment.

To simplify the following derivations, we assume that the two vortex-response variables a_1, a_2 in (A1) are uncoupled (Dghim *et al.* 2021; Bölle 2024). Dropping the indices for convenience, the general solution (A1) then becomes

$$a(t) = \int_{-\infty}^{t} \mathrm{d}s\, e^{-\lambda(t-s)}[\xi(s) + \eta_w(\cos \Omega s + \sin \Omega s)]. \tag{A2}$$

We assume both contributions to the forcing to be random processes, characterising the free stream turbulence and the effect of the free-surface wave, respectively. On the time scale of the vortex response, we suppose the forcing exerted by the free stream turbulence to be a Wiener process (Fontane *et al.* 2008; Bölle 2023). In order to obtain stationary forcing statistics, we assume (Yaglom 1962)

$$\overline{\xi}(t) = \overline{\eta}_w(t) = 0, \quad \overline{\xi^2}(t) = A_t, \quad \overline{\eta_w^2}(t) = A_w, \quad \overline{\xi\eta_w}(t) = 0. \tag{A3}$$

Given the equilibrium solution (A2), the corresponding equilibrium correlation function of the vortex response is

$$\overline{a(s)a(t)} = \int_{-\infty}^{t} \mathrm{d}u\, e^{-\lambda(t-u)} \left[\overline{\eta(u)a(s)} + \overline{\xi(u)a(s)}\right], \tag{A4}$$

on account of the assumed uncorrelatedness of the two forcing contributions.

The equilibrium covariance between wave forcing η and stationary vortex response (A2) is (Yaglom 1962)

$$\overline{\eta(s)a(t)} = A_w \int_{-\infty}^{t} \mathrm{d}u\, e^{-\lambda(t-u)} \cos \Omega(s-u) \tag{A5}$$

$$= A_w e^{-\lambda t} \left[\cos \Omega s \int_{-\infty}^{t} \mathrm{d}u\, e^{\lambda u} \cos \Omega u + \sin \Omega s \int_{-\infty}^{t} \mathrm{d}u\, e^{\lambda u} \sin \Omega u\right]. \tag{A6}$$

Integrating by parts of each of the integrals in (A6) twice and application of the relevant addition theorems yields

$$\overline{\eta(s)a(t)} = A_w \frac{\lambda \cos \Omega(t-s) + \Omega \sin \Omega(t-s)}{\lambda^2 + \Omega^2}. \tag{A7}$$

Injecting this result into (A4), we obtain the equilibrium correlation of the vortex response due to forcing by the free-surface wave

$$\int_{-\infty}^{t} \mathrm{d}u\, e^{-\lambda(t-u)} \overline{\eta(u)a(s)}$$

$$= \frac{A_w e^{-\lambda t}}{\lambda^2 + \Omega^2} \left[\lambda \int_{-\infty}^{t} \mathrm{d}u\, e^{\lambda u} \cos \Omega(s-u) + \Omega \int_{-\infty}^{t} \mathrm{d}u\, e^{\lambda u} \sin \Omega(s-u)\right]. \tag{A8}$$

Using the relevant addition theorems, this can be transformed into a form analogous to (A6). We can then reuse our previous auxiliary relations to obtain the final result

$$\overline{a(s)a(t)}|_{pot} = \frac{A_w}{\lambda^2 + \Omega^2} \cos \Omega(t-s) \tag{A9}$$

for the correlation function due to forcing by the free-surface wave.

The correlation function of the turbulence forcing is assumed to be

$$C(t-s) = \overline{\xi(s)\xi(t)} = A_t \delta_\epsilon(t-s), \tag{A10}$$

whereas δ_ϵ designates a very short correlation such that $\epsilon \ll t$. The correlation magnitude A_t then follows from integration $\int_{\mathbb{R}} \mathrm{d}\tau\, C(\tau) = A_t$. The equilibrium correlation between the random forcing ξ and the stationary vortex response then becomes (Yaglom 1962)

$$\overline{\xi(s)a(t)} = \int_{-\infty}^{t} \mathrm{d}u\, e^{-\lambda(t-u)} \overline{\xi(s)\xi(u)} = \begin{cases} A_t e^{-\lambda(t-s)}, & s < t, \\ 0, & s > t. \end{cases} \tag{A11}$$

With this, the equilibrium correlation due to white-noise random forcing becomes

$$\overline{a(s)a(t)}|_{tur} = \int_{-\infty}^{t} \mathrm{d}u\, e^{-\lambda(t-u)} \overline{f_{tur}(u)a(s)} = \frac{A_t}{2\lambda} e^{-\lambda|t-s|}. \tag{A12}$$

Injecting (A9) and (A12) into (A4) yields the correlation function

$$\overline{a(s)a(t)} = \frac{A_t}{2\lambda} e^{-\lambda|t-s|} + \frac{A_w}{\lambda^2 + \Omega^2} \cos \Omega(t-s) \tag{A13}$$

of the vortex response due to forcing by the free-surface wave and the free stream turbulence.

References

Aguilar-Cabello, J., Parras, L. & del Pino, C. 2022 DPIVSoft-OpenCL: a multicore CPU–GPU accelerated open-source code for 2D Particle Image Velocimetry. *SoftwareX* **20**, 101256.

Archer, P.J., Thomas, T.G. & Coleman, G.N. 2010 The instability of a vortex ring impinging on a free surface. *J. Fluid Mech.* **642**, 79–94.

Arendt, S., Fritts, D.C. & Andreassen, Ø. 1997 The initial value problem for Kelvin vortex waves. *J. Fluid Mech.* **344**, 181–212.

Arnol'd, V.I. 1985 *Ordinary Differential Equations*. MIT Press.

Ash, R.L. & Khorrami, M.R. 1995 Vortex stability. In *Fluid Vortices* (ed. S.I. Green), pp. 317–372. Springer.

Bailey, S.C.C., Pentelow, S., Ghimire, H.C., Estejab, B., Green, M.A. & Tavoularis, S. 2018 Experimental investigation of the scaling of vortex wandering in turbulent surroundings. *J. Fluid Mech.* **843**, 722–747.

Bailey, S.C.C. & Tavoularis, S. 2008 Measurements of the velocity field of a wing-tip vortex, wandering in grid turbulence. *J. Fluid Mech.* **601**, 281–315.

Baker, G.R., Barker, S.J., Bofah, K.K. & Saffman, P.G. 1974 Laser anemometer measurements of trailing vortices in water. *J. Fluid Mech.* **65**, 325–336.

Batchelor, G.K. 2000 *An Introduction to Fluid Dynamics*. Cambridge University Press.

Bölle, T. 2021 Treatise on the meandering of vortices. PhD thesis, Institut Polytechnique de Paris.

Bölle, T. 2023 On the statistics of coherent vortices in incoherent environments. *Physica A* **612**, 128473.

Bölle, T. 2024 On the linear response theory of vortex meandering and its statistical verification in experiments. *J. Fluid Mech.* **997**, A38.

Bölle, T., Brion, V., Couliou, M. & Molton, P. 2023 Experiment on jet–vortex interaction for variable mutual spacing. *Phys. Fluids* **35**, 015117.

Bölle, T., Brion, V., Robinet, J.-C., Sipp, D. & Jacquin, L. 2021 On the linear receptivity of trailing vortices. *J. Fluid Mech.* **908**, A8.

Bühler, O. 2010 Wave–vortex interactions in fluids and superfluids. *Annu. Rev. Fluid Mech.* **42**, 205–228.

Chen, T. & Chwang, A.T. 2002 Trailing vortices in a free-surface flow. *Phys. Fluids* **14**, 827–838.

Curtis, C.W. & Kalisch, H. 2017 Vortex dynamics in nonlinear free surface flows. *Phys. Fluids* **29**, 032101.

Del Pino, C., Parras, L., Felli, M. & Fernandez-Feria, R. 2011 Structure of trailing vortices: comparison between particle image velocimetry measurements and theoretical models. *Phys. Fluids* **23** (1), 013602.

Devenport, W.J., Rife, M.C., Liapis, S.I. & Follin, G.J. 1996 The structure and development of a wing-tip vortex. *J. Fluid Mech.* **312**, 67–106.

Dghim, M., Ben Miloud, K., Ferchichi, M. & Fellouah, H. 2021 Meandering of a wing-tip vortex in a grid-generated turbulent flow. *Phys. Fluids* **33**, 115131.

Dghim, M., Ferchichi, M. & Fellouah, H. 2020 On the effect of active flow control on the meandering of a wing-tip vortex. *J. Fluid Mech.* **896**, A30.

Edstrand, A.M., Davis, T.B., Schmid, P.J., Taira, K. & Cattafesta, L.N. 2016 On the mechanism of trailing vortex wandering. *J. Fluid Mech.* **801**, R1.

Fabre, D. 2002 Instabilités et instationnarités dans les tourbillons: application aux sillage d'avions. PhD thesis, Université Paris VI.

Fabre, D. & Jacquin, L. 2004 Viscous instabilities in trailing vortices at large swirl numbers. *J. Fluid Mech.* **500**, 239–262.

Fabre, D., Sipp, D. & Jacquin, L. 2006 Kelvin waves and the singular modes of the Lamb–Oseen vortex. *J. Fluid Mech.* **551**, 235–274.

Fontane, J., Brancher, P. & Fabre, D. 2008 Stochastic forcing of the Lamb–Oseen vortex. *J. Fluid Mech.* **613**, 233–254.

Garrido-Martin, M., Blanco-Rodríguez, F.J., Gutierrez-Castillo, P., Bölle, T. & del Pino, C. 2025 Frequency response analysis of jet–vortex interaction for variable relative spacing. *Phys. Fluids* **37**, 034103.

Gutierrez-Castillo, P., Garrido-Martin, M., Bölle, T., García-Ortiz, J.H., Aguilar-Cabello, J. & del Pino, C. 2022 Higher order dynamic mode decomposition of an experimental trailing vortex. *Phys. Fluids* **34**, 107116.

HEYES, A.L., JONES, R.F. & SMITH, D.A.R. 2004 Wandering of wing-tip vortices. In *Proceedings of the 12th International Symposium on Applications of Laser Techniques to Fluid Mechanics*, pp. 35–33.

HOLMES, P., LUMLEY, J.L. & BERKOOZ, G. 1996 *Turbulence, Coherent Structures, Dynamical Systems and Symmetry*. Cambridge University Press.

IBRAHIM, R.A. 2005 *Liquid Sloshing Dynamics: Theory and Applications*. Cambridge University Press.

JACQUIN, L., FABRE, D., GEFFROY, P. & COUSTOLS, E. 2001 The properties of a transport aircraft wake in the extended far field: an experimental study. *AIAA Paper* 2001-1038.

KARAMI, M., HANGAN, H., CARASSALE, L. & PEERHOSSAINI, H. 2019 Coherent structures in tornado-like vortices. *Phys. Fluids* **31**, 085118.

LANDAU, L.D. & LIFSHITZ, E.M. 1987 *Fluid Mechanics - Course of Theoretical Physics*, vol. 6. Pergamon Press.

LINDEN, P.F. 1973 The interaction of a vortex ring with a sharp density interface: a model for turbulent entrainment. *J. Fluid Mech.* **60**, 467–480.

MARSHALL, J.S. & BENINATI, M.L. 2005 External turbulence interaction with a columnar vortex. *J. Fluid Mech.* **540**, 221–245.

MCINTYRE, M.E. 2019 Wave–vortex interactions, remote recoil, the Aharonov–Bohm effect and the Craik–Leibovich equation. *J. Fluid Mech.* **881**, 182–217.

MELANDER, M.V. & HUSSAIN, F. 1993 Coupling between a coherent structure and fine-scale turbulence. *Phys. Rev. E* **48**, 2669–2689.

MEUNIER, P. & LEWEKE, T. 2003 Analysis and treatment of errors due to high velocity gradients in particle image velocimetry. *Exp. Fluids* **35**, 408–421.

MOORE, D.W. & SAFFMAN, P.G. 1973 Axial flow in laminar trailing vortices. *Proc. R. Soc. Lond. A* **333**, 491–508.

NORTH, G.R. 1984 Empirical orthogonal functions and normal modes. *J. Atmos. Sci.* **41**, 879–887.

POINCARÉ, H. 1893 *Théorie des Tourbillons*. Gauthier-Villars.

PRADEEP, D.S. & HUSSAIN, F. 2010 Vortex dynamics of turbulence–coherent structure interaction. *Theor. Comput. Fluid Dyn.* **24**, 265–282.

QIU, S., CHENG, Z., XU, H., XIANG, Y. & LIU, H. 2021 On the characteristics and mechanism of perturbation modes with asymptotic growth in trailing vortices. *J. Fluid Mech.* **918**, A41.

ROY, C., LEWEKE, T., THOMPSON, M.C. & HOURIGAN, K. 2011 Experiments on the elliptic instability in vortex pairs with axial core flow. *J. Fluid Mech.* **677**, 383–416.

ROY, A. & SUBRAMANIAN, G. 2014 Linearized oscillations of a vortex column: the singular eigenfunctions. *J. Fluid Mech.* **741**, 404–460.

SAFFMAN, P.G. 1995 *Vortex Dynamics*. Cambridge University Press.

SARPKAYA, T. & NEUBERT, D.E. 1994 Interaction of a streamwise vortex with a free surface. *AIAA J.* **32**, 594–600.

SARPKAYA, T. & SUTHON, P. 1991 Interaction of a vortex couple with a free surface. *Exp. Fluids* **11**, 205–217.

TENNEKES, H. & LUMLEY, J.L. 1972 *A First Course in Turbulence*. MIT Press.

VAN HEIJST, G.J.F. 2017 Effects of rotation and stratification: an introduction. In *Mixing and Dispersion in Flows Dominated by Rotation and Buoyancy* (ed. H.J.H. Clercx & G.J.F. van Heijst), pp. 1–24. Springer.

VAN JAARSVELD, J.P.J., HOLTEN, A.P.C., ELSENAAR, A., TRIELING, R.R. & VAN HEIJST, G.J.F. 2011 An experimental study of the effect of external turbulence on the decay of a single vortex and a vortex pair. *J. Fluid Mech.* **670**, 214–239.

VON STORCH, H. & ZWIERS, F.W. 2003 *Statistical Analysis in Climate Research*. Cambridge University Press.

WILKS, D.S. 1997 Resampling hypothesis tests for autocorrelated fields. *J. Climate* **10**, 65–82.

WILKS, D.S. 2006 *Statistical Methods in the Atmospheric Sciences*. Academic Press.

WU, Y., XIAO, Z., XIANG, Y., LI, D. & LIU, H. 2025 The response and receptivity mechanism of wingtip vortex under the effect of external disturbance. *Phys. Fluids* **37**, 037162.

YAGLOM, A.M. 1962 *An Introduction to the Theory of Stationary Random Functions*. Prentice Hall.